Hierarchical Heterogeneity across Human Cortex Shapes Large-Scale Neural Dynamics

Murat Demirta [1], **Joshua B. Burt**[2,7], **Markus Helmer**[1,7], **Jie Lisa Ji**[1], **Brendan D. Adkinson**[1], **Matthew F. Glasser**[3,4], **David C. Van Essen**[3], **Stamatios N. Sotiropoulos**[5,6], **Alan Anticevic**[1], and **John D. Murray**[1,2,8,*]

[1]Department of Psychiatry, Yale University School of Medicine, New Haven, CT, USA

[2]Department of Physics, Yale University, New Haven, CT, USA

[3]Department of Neuroscience, Washington University School of Medicine, Saint Louis, MO, USA

[4]St. Luke's Hospital, Saint Louis, MO, USA

[5]Sir Peter Mansfield Imaging Centre, School of Medicine, University of Nottingham, Nottingham, UK

[6]Wellcome Centre for Integrative Neuroimaging, Centre for Functional MRI of the Brain, Nuffield Department of Clinical Neuroscience, John Radcliffe Hospital, University of Oxford, Oxford, UK

[7]These authors contributed equally

[8]Lead Contact

SUMMARY

The large-scale organization of dynamical neural activity across cortex emerges through long-range interactions among local circuits. We hypothesized that large-scale dynamics are also shaped by heterogeneity of intrinsic local properties across cortical areas. One key axis along which microcircuit properties are specialized relates to hierarchical levels of cortical organization. We developed a large-scale dynamical circuit model of human cortex that incorporates heterogeneity of local synaptic strengths, following a hierarchical axis inferred from magnetic resonance imaging (MRI)-derived T1- to T2-weighted (T1w/T2w) mapping and fit the model using multimodal neuroimaging data. We found that incorporating hierarchical heterogeneity substantially improves the model fit to functional MRI (fMRI)-measured resting-state functional connectivity and captures sensory-association organization of multiple fMRI features. The model predicts hierarchically organized higher-frequency spectral power, which we tested with resting-

state magnetoencephalography. These findings suggest circuit-level mechanisms linking spatiotemporal levels of analysis and highlight the importance of local properties and their hierarchical specialization on the large-scale organization of human cortical dynamics.

In Brief

Demirta et al. report a large-scale circuit model of human cortex incorporating regional heterogeneity in microcircuit properties using T1w/T2w mapping for parametrization across the cortical hierarchy and fitting models to resting-state functional connectivity. This study shows that hierarchical heterogeneity provides an organizing principle for spatiotemporal dynamics of human cortex.

INTRODUCTION

Spatiotemporal dynamics of a neural system are shaped by structural constraints on interactions among the system's components, as well as intrinsic dynamical properties of those components. An open question in systems neuroscience is how areal heterogeneity of local circuit properties across cortex shapes large-scale structure-function relationships. Hierarchical organization provides a parsimonious principle for anatomical properties of inter-areal connections in primate cortex (Felleman and Van Essen, 1991; Dombrowski et al., 2001; Markov et al., 2014). Anatomically defined cortical hierarchy aligns with sensory processing hierarchies, with early sensory areas at lower levels and association areas at higher levels (Felleman and Van Essen, 1991; Markov et al., 2014). Functional and dynamical properties (Murray et al., 2014; Honey et al., 2012), as well as specialization of cortical microcircuitry (Burt et al., 2018; Chaudhuri et al., 2015), vary across hierarchical levels, yet it is unclear how hierarchical specialization of local circuit properties across human cortex shapes the large-scale organization of neural dynamics.

Advances in magnetic resonance imaging (MRI) have provided noninvasive methods for characterizing large-scale connectivity in the human brain at the structural and functional levels. Structural connectivity (SC) is often inferred from diffusion MRI (dMRI), which aims to quantify the density of anatomical fibers linking brain regions. The functional organization of human brain activity has been studied most extensively through functional MRI (fMRI) measurements of blood-oxygen-level-dependent (BOLD) signals. Resting-state functional connectivity (rs-FC) provides a measure of temporal correlations in spontaneous activity between regions and has revealed an intrinsic architecture of the human brain (Cole et al., 2014). Recent findings suggest that hierarchy may be a useful principle for rs-FC patterns in human cortex (Margulies et al., 2016), including capturing sensory-association differences in inter-individual variation (Mueller et al., 2013; Finn et al., 2015) and dysfunction in disease states (Baker et al., 2014; Yang et al., 2016).

Computational models of large-scale brain circuits propose dynamical circuit mechanisms linking the structural and functional organization of human cortex. In a major class of biophysically based dynamical models, large-scale patterns of rs-FC arise through physiological dynamics of local cortical circuits interconnected through long-range structural connections (Deco et al., 2011; Breakspear, 2017). Importantly, simulated

functional connectivity (FC) in these models is shaped by the physiological properties of the local circuits, such as strengths of excitatory and inhibitory synaptic connections (Deco et al., 2013, 2014; Yang et al., 2014). However, the role of inter-areal heterogeneity of local circuit properties has not been systematically studied in large-scale models of human cortex.

Microcircuit specialization across human cortex can be informed by structural neuroimaging measures of cortical architectural variation. In particular, the MRI-derived contrast ratio of T1- to T2-weighted (T1w/T2w) maps has been proposed to provide an *in vivo* measure of intracortical myelin content (Glasser and Van Essen 2011; Glasser et al., 2014). Cortical myelin content has been observed to correlate with a prominent sensory-association gradient in rs-FC variation (Margulies et al., 2016; Huntenburg et al., 2017). Burt et al. (2018) found that the T1w/T2w map provides a noninvasive neuroimaging proxy measure of anatomical hierarchy in primate cortex. Multiple aspects of hierarchical specialization, including in excitatory and inhibitory microcircuitry, vary along this cortical axis. In the human cortex, the T1w/T2w map captures the dominant areal pattern of variation in gene expression (Burt et al., 2018). We hypothesized that hierarchical specialization of local microcircuitry across human cortex, as captured by T1w/T2w maps, shapes the large-scale organization of rs-FC.

To address these issues, we developed a large-scale cortical circuit model incorporating hierarchical heterogeneity of local microcircuit properties and quantitatively fit the model using multimodal human neuroimaging data from the Human Connectome Project (HCP) (Van Essen et al., 2013). We used the T1w/T2w map to parametrize hierarchical heterogeneity in local synaptic strengths across cortical areas. Compared to a model with homogeneous microcircuit properties across areas, this heterogeneous model better captured empirical rs-FC patterns, with the T1w/T2w map providing a preferential axis for areal heterogeneity. Furthermore, the model predicts a hierarchical axis of specialization for spectral features of higher-frequency neural dynamics, which we found to be consistent with resting-state magnetoencephalography (MEG). Our study provides a computational framework to study how areal specialization of microcircuitry shapes large-scale network function of the human brain, opening applications to neuropsychiatric disorders and pharmacological effects.

RESULTS

We first describe the computational framework for the large-scale circuit model of human cortex, incorporating areal heterogeneity of local properties, which we applied to the HCP multimodal neuroimaging dataset from a large number of healthy subjects (n = 334) (Figure 1A). The cortical surface was parcellated into multiple contiguous areas. Here, we applied a recently developed multimodal parcellation from the HCP, which yielded 180 cortical areas per hemisphere (Glasser et al., 2016). Each cortical area was modeled as a local circuit comprising excitatory pyramidal neurons and inhibitory interneurons coupled through recurrent synaptic interactions, with neurophysiologically interpretable parameters governing local dynamics, as described below. Areas in the large-scale network interact via structured long-range excitatory projections constrained by a matrix, derived here from dMRI and probabilistic tractography (Figure S1). We simulated only within-hemisphere interactions to focus model fitting on capturing the network structure of rs-FC and because

dMRI is limited in mapping callosal projections. The SC matrix thereby provides a structural scaffold for long-range neural interactions in the model.

The model simulates time-varying activity of excitatory and inhibitory neuronal populations in a local circuit for each cortical area. For computational tractability of model fitting, as well as mathematical analysis of the system, we used a reduced mean-field approximation of synaptic dynamics for each neuronal population in the network (Wong and Wang, 2006; Deco et al., 2013, 2014). Populations receive synaptic input from multiple sources, with contributions from the fluctuating background, local recurrent connections, and long-range connections from other areas, which induces structured correlated fluctuations across the network. Each local node is characterized by two synaptic parameters, which set the strengths of local excitatory-to-excitatory (W^{EE}) and excitatory-to-inhibitory (W^{EI}) connections. The inhibitory-to-excitatory strength (W^{IE}) was set to maintain a uniform baseline firing rate, dependent on theother parameters (Deco et al., 2014) (Tables 1 and 2). Global coupling parameters $g_{\{L,R\}}$ scale the strengths of long-range interactions within the left and right hemispheres. Synaptic activity is used to simulate the BOLD signal using the mechanistic Balloon-Windkessel model for the hemodynamic response (Friston et al., 2003; Deco et al., 2013). The model can thereby yield a simulated BOLD FC matrix, which can be compared to empirical BOLD rs-FC data. The neurophysiological model parameters can then be optimized to provide the best fit to empirical rs-FC.

A key extension to the model framework introduced here is a hypothesis-driven approach to incorporate areal heterogeneity of local circuit properties (Figure 1B). We compared performance of the circuit model with homogeneous and heterogeneous local circuit parameters. In the "homogeneous" model, synaptic parameters were uniform across cortical areas, and its four parameters were optimized globally (W^{EE}, W^{EI}, g_L, and g_R). In contrast, in the "heterogeneous" model, parameter values (here, W^{EE} and W^{EI}) can vary across cortical areas, parametrized according to a predefined heterogeneity map. The heterogeneity map thereby constrains the topography of local circuit specialization in the heterogeneous model.

T1w/T2w as a Hierarchical Heterogeneity Map

We hypothesized that cortical hierarchy provides a principle describing specialization of microcircuit properties across cortical areas that shapes large-scale functional dynamics. We therefore sought to implement the model with a heterogeneity map that reflects a hierarchical ordering of cortical areas. Because anatomical hierarchy is derived through invasive tract-tracing, which has precluded direct investigation in human cortex, we sought a noninvasive proxy measure. Burt et al. (2018) found that the MRI-derived T1w/T2w map is negatively correlated with anatomical hierarchy in macaque cortex and that specialization in multiple aspects of cortical microcircuitry were found to correlate with the T1w/T2w map (Figure 1C). In particular, they found a negative correlation between T1w/T2w values and the number of spines on pyramidal cell dendrites, which can be interpreted as a microanatomical correlate of recurrent excitatory synaptic strengths (Elston, 2003; Chaudhuri et al., 2015), suggesting stronger values of W^{EE} in association areas with low T1w/T2w values.

In human cortex, areas can be contextualized in terms of coherent resting-state networks (RSNs) associated with different sensory and higher-order association functions. We assigned all areas to 8 canonical RSNs comprising three sensory networks (visual, somatosensory, and auditory) and five association networks (frontoparietal, cingulo-opercular, default mode, dorsal attention, and ventral attention) (Ito et al., 2017) (Figure 1D). We observed that T1w/T2w map values were significantly higher in sensory networks than in association networks ($p < 0.003$, Wilcoxon signed-rank test) (Burt et al., 2018) (Figure 1E). In further support of the T1w/T2w map as a proxy measure of hierarchical microcircuit specialization across human cortex, Burt et al. (2018) analyzed the topography of cortical gene expression and found that the T1w/T2w map captures the dominant spatial pattern of gene expression variation in human cortex.

These findings suggest that the T1w/T2w map may capture a key axis of areal heterogeneity across cortex, which we quantitatively instantiated in the model. We derived a hierarchical heterogeneity map by rescaling and inverting the raw T1w/T2w map, such that its values are relatively uniformly distributed between 0 and 1, with high-T1w/T2w sensory areas at low map values and low-T1w/T2w association areas at high map values (Figure S2). Local synaptic strengths (W^{EE} and W^{EI}) were then parametrized for each area i as an affine function of the heterogeneity map values {h_i}, characterized by an intercept w_{min} and scale factor W_{scale}: $W_i = W_{min} + W_{scale}h_i$ (Figure 1B). Use of a heterogeneity map in model fitting thereby enables hypothesis-driven investigation of areal differences in local circuit properties while increasing model complexity by only a single additional parameter for each heterogeneous property.

Model Fitting

We quantitatively fit the models described above to rs-FC data. To estimate the optimal model parameter values, we used hierarchical population Monte Carlo (hPMC), a Bayesian optimization technique (Figure S2C). hPMC approximates the posterior distribution in parameter space by iteratively drawing a set of model parameters (i.e., "particles") from the proposed distribution to minimize a distance measure between model and empirical data. We fit the model parameters to maximize the average Pearson correlation between model and empirical FC across subjects (n = 334). To calculate the model FC, we used an analytical approximation of linearized system dynamics, which enables computationally efficient calculation of dynamical features of the system, including the FC matrix (Deco et al., 2013, 2014) (Figure S3). Here, we extended this approach to include linearization of the Balloon-Windkessel hemodynamic model for direct calculation of the BOLD FC matrix. This analytical calculation of BOLD FC provided computational efficiency needed for parameter fitting while producing a highly accurate estimate of simulated BOLD FC ($r = 0.972 \pm 0.005$ for simulations of duration ~1 h, i.e. 4,800 repetition times [TRs]) (Figure S3). The fitting procedure produced the approximated posterior distribution of the optimal model parameters. To assess parameter identifiability, we performed hPMC fitting on model-generated FC matrices from the approximate posterior of the heterogeneous model. The fitting procedure recovered parameters well, with and without observation noise over the objective FC (Figure S4).

Hierarchical Heterogeneity Improves Fit to FC

We tested whether hierarchical heterogeneity improves similarity between empirical rs-FC and fit model FC patterns compared to a homogeneous model with uniform properties across cortical areas. Figures 2A–2D show empirical group-averaged SC and FC matrices and particle-averaged FC matrices for the homogeneous and heterogeneous models. We quantified model performance using the goodness of fit (i.e., squared Pearson correlation coefficient) of empirical FC, averaged across subjects, captured by the model FC, averaged across samples from the approximate posterior distribution. We found that the similarity between empirical and model FC was significantly higher in the heterogeneous model ($r = 0.560$, $r^2 = 0.313$) than in the homogeneous model ($r = 0.407$, $r^2 = 0.166$) ($p < 10^{-4}$, dependent correlation test) (Figure 2G). Both models yielded higher FC similarity compared to the SC-FC similarity as a baseline ($r = 0.284$, $r^2 = 0.081$) ($p < 10^{-4}$, dependent correlation test).

The fit between SC and model FC was significantly lower for the heterogenous model ($r = 0.440$, $r^2 = 0.190$) than the homogeneous model ($r = 0.595$, $r^2 = 0.354$) ($p < 10^{-4}$, dependent correlation test), which suggests that areal heterogeneity can help to explain FC patterns not accounted for by SC (Chaudhuri et al., 2015). We tested this suggestion with a multiple regression model of FC with SC as an additional predictor. Regression coefficients of both models were significant ($p < 10^{-4}$. However, the heterogeneous model FC improved the explained variance by 20% relative to a reduced model including only SC, compared to only 3% for the homogeneous model.

The optimal fit parameters for the heterogenous model exhibited a large scaling of local recurrent excitatory-to-excitatory synaptic strengths (W^{EE}) across the hierarchical heterogeneity map $\left(W^{EE}_{scale} / W^{EE}_{min} \approx 0.89 \right)$ (Figure 2H). We tested the impact of hierarchical heterogeneity in other, non-weight parameters, specifically the excitatory and inhibitory time constants (i.e., τ_E and τ_I). This model did not outperform the heterogeneous model based on synaptic weights ($r = 0.45$; $p < 10^{-4}$, dependent correlation test). We also investigated hierarchical heterogeneity of local self-coupling in more abstract dynamical models, specifically an Ornstein-Uhlenbeck (OU) model and a simultaneous autoregressive (SAR) model. For both models, heterogeneity substantially improved model fit (OU: $r = 0.517$ for heterogeneous versus $r = 0.419$ for homogeneous; SAR: $r = 0.504$ versus $r = 0.414$), but neither outperformed the heterogeneous circuit model ($p < 10^{-4}$, dependent correlation test).

To provide mechanistic insight into the models, we examined the eigenvalues and eigenvectors of the linearized dynamical system (Figure S5). In the homogeneous model, the leading eigenvectors (i.e., with largest eigenvalues and longest timescales) exhibited a global activation pattern, whereas the heterogeneous model showed spatially structured leading eigenvectors. These leading eigenvectors exhibited a network-dependent hierarchical organization rather than a strictly monotonic relationship with the T1w/T2w. The slowest eigenvector weights showed a strong positive correlation with T1w/T2w map in the visual RSN, but not globally, peaking at lateral inferior parietal and lateral prefrontal cortex, consistent with the visual hierarchical organization.

Because the heterogeneous model has more parameters than the homogeneous model (6 versus 4), we tested that fit improvement was not due to over-fitting with the more expressive model. Implementing repeated random subsampling cross-validation, we repeated the fitting procedure for a randomly selected subset of 80% of the subjects (267), and measured the model fit to the remaining 20% of subjects (67). Across 100 cross-validation samples, the predictive power of the heterogeneous model ($r = 0.548 \pm 0.01$) always outperformed the homogeneous model ($r = 0.405 \pm 0.005$).

In addition, we tested whether the improved model fit in the heterogeneous model can be explained by known non-neural confounds in rs-fMRI, such as head motion, variations in heart rate, and respiration. If the improved fit of the heterogeneous model is due to its capture of non-neural FC contributions, then individual differences in non-neural measures should explain individual differences in the improvement in empirical-model FC similarity for heterogeneous versus homogeneous models. The heterogeneous model improved the FC fit for 98.5% of the 334 subjects. We performed a regression analysis across subjects on the difference in model-empirical fit between heterogeneous and homogeneous models. A constant term (i.e., without non-neural measures) explained 80% of the total sum of squares, and inclusion of individual non-neural measures improved the explained variance by only 1.5%. This suggests that the substantial improvement in fitting by the heterogeneous model is not attributable to non-neural confounds.

T1w/T2w Map as Preferential Axis of Areal Specialization

Does the T1w/T2w-based hierarchical heterogeneity map provide a preferential axis of cortical specialization in comparison to other possible heterogeneity maps? To address this question, we repeated the model fitting procedure for a single hemisphere using the T1w/T2w-based heterogeneity map and 500 randomized surrogate heterogeneity maps. Because T1w/T2w map values are spatially autocorrelated, we developed a procedure to generate surrogate maps that randomly vary in their particular topographies but preserve the general spatial autocorrelation structure of the T1w/T2w-based map (Figures 3A–3C).

We found that the model fit of the surrogate maps was slightly higher than that of the homogeneous model, with an average correlation $r = 0.44$ for surrogates versus $r = 0.41$ for the homogeneous model. Nonetheless, among all surrogate maps, the T1w/T2w-derived map exhibited significantly higher model fit than surrogates ($p = 0.008$, $r = 0.55$ for the heterogenous model) (Figure 3D). Furthermore, the model fit using surrogate heterogeneity maps was significantly correlated with their similarity to the T1w/T2w-based heterogeneity map (Figure 3E). To test the importance of finer gradients within the T1w/T2w map, we tested an alternative model with a heterogeneity map defined by two categorical levels for sensory versus association networks. This categorical model performed better than the homogeneous model but worse than the T1w/T2w-based heterogeneity map model ($r = 0.51$; $p < 10^{-4}$ for both, dependent correlation test). These findings suggest that the T1w/T2w map provides a preferential neural axis for cortical microcircuit specialization, in line with prior empirical characterization of microanatomical and transcriptional specialization along the T1w/T2w map (Burt et al., 2018).

Model Fit across RSNs

We examined how the improved performance of the hierarchical heterogeneous model was distributed across different functionally relevant cortical networks and whether this was due to capturing rs-FC patterns within networks or across networks. We calculated the model-empirical FC similarity for each of eight RSNs (three sensory, five association), decomposing its FC pattern into within-network and across-network components (Figures 4A and 4D). We found that both within- and across-network fits to empirical FC were higher in the heterogeneous model than in the homogeneous model for all RSNs (Figures 4B–4F), with association RSNs showing a larger improvement than sensory RSNs in within-network similarity. Among the association RSNs, the frontoparietal (FPN) and cingulo-opercular (CON) networks exhibited large increases in both within- and across-network fits. These results show that incorporating hierarchical heterogeneity not only improves the whole-cortex model FC fit but also preferentially improves the within-network model FC fit in association networks.

Global Brain Connectivity

The RSN analyses presented above suggest that hierarchical heterogeneity may allow the model to capture important rs-FC differences between sensory and association networks. To investigate sensory-association differences more directly, we studied the topography of global brain connectivity (GBC), a measure of global FC strength for each area (Figure 5A). Studies have found GBC to be an informative measure of rs-FC alterations in psychiatric disorders (Cole et al., 2011; Yang et al., 2016) and individual differences in cognition (Cole et al., 2012). Furthermore, there is evidence that the cortical topography of pharmacologically induced changes in GBC is aligned with the topography of gene expression for the targeted receptor (Preller et al., 2018). We therefore examined whether hierarchical heterogeneity of circuit properties in the model shapes the cortical GBC topography in healthy subjects.

We found that GBC, calculated within cortex, was significantly different across sensory and association RSNs, with higher GBC in sensory areas than in association areas ($p < 0.003$, Wilcoxon signed-rank test) (Figures 5B and 5C). The correlation with empirical GBC was significantly higher for the heterogeneous model ($r_s = 0.743$) than that for the homogeneous model ($r_s = 0.482$) ($p < 10^{-4}$, dependent correlation test) (Figures 5D–5F). Notably, SC input strengths are normalized such that the net in-degree is homogeneous across nodes, in both models. We further assessed these results by examining relationships between model GBC, degree of the binarized SC graph, and weights of the slowest eigenvectors (Figures S5N–S5P). The homogeneous model GBC was strongly correlated with degree of binarized SC ($r_s = 0.680$) (Baria et al., 2013). In contrast, the heterogeneous model GBC was mostly driven by the eigenvector of the slowest Jacobian mode ($r_s = 0.933$. These findings suggest that hierarchical heterogeneity of local circuit properties may play a role in shaping sensory-association differences in the large-scale organization of rs-FC.

Inter-individual Variation

Cortical rs-FC patterns vary across individuals. Mueller et al. (2013) characterized the degree to which cortical areas vary in their FC profiles across subjects and found a marked

hierarchical difference across RSNs; sensorimotor regions exhibited low inter-individual variation in FC, whereas association regions exhibited higher variation. As noted above, our model fitting approach uses hPMC to fit a posterior distribution in parameter space to the full set of FC patterns across subjects in the HCP dataset. Of note, particles share the same structural connectivity matrix and heterogeneity map and differ only in their synaptic parameter values. We can therefore study whether the best-fit model exhibits hierarchical differences in FC variation across particles drawn from the approximated posterior distribution, comparable to the FC variation across subjects in the empirical data.

We quantified the variability within the population as the dissimilarity of FC patterns across individuals, following the approach of Mueller et al. (2013). In the model, the dissimilarity of FC patterns was calculated across 1,000 particles that were sampled from the posterior distribution (Figure 6A). In this study, model particles all used the same SC matrix, averaged over subjects. This allowed our analyses to isolate potential contributions to individual variation in rs-FC arising from variation in physiological circuit properties. We note this is one potential source of variation and that individual differences in SC likely also shape differences in FC (Zimmermann et al., 2019).

Across the 334 subjects, we found that the inter-individual dissimilarity was higher in frontal and temporal brain regions (Figure 6B). The inter-individual dissimilarity in association RSNs was on average higher than in sensory RSNs ($p < 0.003$, Wilcoxon signed-rank test; Z score 0.265 ± 1.055 and 0.659 ± 0.410 for association and sensory RSNs, respectively). Similar to the empirical data, the heterogeneous model showed higher inter-particle dissimilarity in frontal association areas (Figure 6C). The topography of empirical dissimilarity was positively and moderately correlated with that of the heterogeneous model ($r = 0.491$), unlike with the homogeneous model ($r = -0.08$). The heterogeneous model exhibits a similar hierarchical distinction in dissimilarity, with higher inter-particle variability in association regions than in sensory regions, whereas no such pattern is present in the homogeneous model ($p < 0.0001$, network $\times$ model type ANOVA, $z = 5.30$) (Figure 6D). We also compared the SD of each FC connection across subjects or particles and found that the model-empirical similarity of this measure was higher for the heterogeneous model than for the homogeneous model ($r = 0.521$ versus $r = 0.305$; $p < 10^{-4}$, dependent correlation test).

Incorporation of heterogeneity expanded the dimensionality of fitting to the empirical population (Figures 6F–6I). We applied principal-component analysis (PCA) to the distribution of model particles from the hPMC fitting in the fit parameter space. The homogeneous model exhibited only a single axis of particle variation in its four-dimensional parameter space, indicating one-dimensional expressiveness of the synaptic parameters. In contrast, the heterogeneous model exhibited four effective dimensions of variation in its six-dimensional parameter space. Hierarchical heterogeneity of local recurrent strengths therefore contributes degrees of freedom that substantially increase model expressiveness. These findings suggest that hierarchical heterogeneity may contribute to individual variation in the functional organization of cortex.

Heterogeneity in Neural Dynamics across Multiple Timescales

How does hierarchical heterogeneity in the model shape neural dynamics across a wide range of timescales? The results described above examined simulated BOLD signals from a hemodynamic model that are driven by synaptic activity in the neural circuits. Cortical areas differ in the spectral properties of their intrinsic dynamics at rest (Honey et al., 2012; Murray et al., 2014; Keitel and Gross, 2016; Mellem et al., 2017). In local circuit models, synaptic strengths can shape these spectral properties (Chaudhuri et al., 2015; Murray et al., 2017). We therefore sought to examine in the model how hierarchical heterogeneity produces specific areal topographies of neural dynamics across multiple timescales.

We first characterized the dynamical repertoire of the local microcircuit model at each node in the large-scale network as a function of the recurrent excitatory strengths onto excitatory and inhibitory neurons: W^{EE} and W^{EI} (Figures 7A and S6). As W^{EE} increases, there is a threshold value (i.e., a bifurcation point) beyond which the system's baseline state destabilizes (Deco et al., 2013). When W^{EI} is large, the system exhibits another dynamical regime in which the system's dynamics undergo damped oscillations. In the heterogeneous model, areas are hierarchically dispersed along a line in the (W^{EE}; W^{EI}) parameter space, whereas in the homogeneous model, all areas are set at the same point. We found that the optimal parameters of both models were close to the bifurcations (Figures 7B and 7C), in line with prior studies (Deco et al., 2013, 2014).

We characterized the power spectral density (PSD) of the underlying synaptic activity in the models (Figures 7D and 7E). The homogeneous model exhibits PSDs that did not differ substantially across areas. In contrast, the heterogeneous model exhibits gradual shifts in PSD profiles across hierarchical levels. To examine the contributions of inter-areal connectivity to these dynamics, we simulated the effect of "disconnection" in the network (Figure S7). We found that long-range connections primarily shape low-frequency power (<1 Hz), suggesting differential contribution of local and long-range inputs in shaping spectral features. Distance-dependent synaptic delays in long-range projections did not substantially affect simulated PSD or BOLD FC patterns (Figure S7). These results suggest that hierarchical heterogeneity shapes the spatial topography of spectral features across multiple timescales.

MEG PSD

We tested the model prediction that spectral features are hierarchically organized using the PSD from resting-state MEG. The empirical MEG-derived PSD of many areas exhibits a prominent alpha-band peak with a posterior-anterior topography (Figure 8A). To remove strong topographic effects of alpha- and beta-band peaks, we fit the MEG PSD to its 0-Hz, alpha and beta peak Lorentzians and removed the alpha and beta Lorentzians from the PSD (Figures 8B and S8). We then performed PCA on the normalized PSDs (see STAR Methods). The first principal axis is the spectral pattern that captures the most variation in PSDs across areas (67.5% for the empirical MEG) (Figure 8C). The first principal component (PC-1) is the areal map whose values are the loadings of spectral variation for each area onto the first principal axis (Figure 8D). We found that the PC-1 map was significantly correlated with the T1w/T2w map ($r_s = 0.631$, $p = 0.002$, against 500

randomized surrogate maps with matching spatial autocorrelation). These results show that spectral features in resting-state MEG exhibits topographic signatures of hierarchical heterogeneity across cortical areas, in line with model predictions.

We also performed the same PCA procedure on the PSDs of the heterogeneous and homogeneous models (Figures 8E–8G and S8). The correlation between empirical and model PC-1 topographies was significantly higher for the heterogeneous model ($r_s = 0.631$) than for the homogeneous model $r_s = 0.138$ ($p < 10^{-4}$, dependent correlation test). These results suggest that the hierarchical organization of cortical circuits may shape the large-scale organization of spectral features across a range of timescales.

DISCUSSION

In this study, we proposed a biophysically based large-scale dynamical model of human cortical activity that incorporates hierarchical heterogeneity in local circuit properties. We hypothesized that the T1w/T2w map would provide a key neural axis along which microcircuit properties and spatiotemporal dynamics would vary. This hypothesis was informed by a convergence of findings across multiple modalities linking the T1w/T2w map, microcircuit specialization, functional organization, and the organizing principle of cortical hierarchy. Incorporating hierarchical heterogeneity in local circuit properties substantially improved the model fit to BOLD rs-FC and captured the sensory-association organization of multiple fMRI features. The heterogeneous model predicted a hierarchical topography of higher-frequency spectral features, which we found to be present in MEG. Collectively, our findings suggest that heterogeneity in local circuit properties shapes the large-scale organization of neural dynamics in human cortex.

The T1w/T2w map captures a number of aspects of microcircuit specialization across cortex. This structural MRI-derived contrast measure is sensitive to regional variation in multiple microstructural properties, including intracortical myelin content (Glasser et al., 2014, 2016). Burt et al. (2018) found that the T1w/T2w map captures areal variation in cytoarchitecture (Hilgetag et al., 2016), cell-type distributions, and synaptic properties. The number and density of dendritic spines on pyramidal neurons, a microanatomical correlate of local synaptic excitation, increase with cortical hierarchy, as captured by the T1w/T2w map (Elston, 2003; Glasser et al., 2014; Chaudhuri et al., 2015; Burt et al., 2018). This observation provides microanatomical support for our heterogeneous model's local recurrent excitatory strengths following an increasing hierarchical gradient (Chaudhuri et al., 2015). Furthermore, large-scale gene expression mapping of human cortex reveals that the T1w/T2w map captures the dominant neural axis of transcriptional variation, suggesting a common hierarchical organization for functional specialization (Burt et al., 2018). These findings support our use of the T1w/T2w map as a key neural axis for hierarchical microcircuit specialization.

Electrophysiological studies have established that functional dynamics of cortical areas also exhibit an organization along a sensory-association hierarchy. The timescales of intrinsic fluctuations vary across hierarchical levels both in humans (Honey et al., 2012) and in monkeys at the single-neuron level (Murray et al., 2014). Computational modeling studies

have demonstrated that these differences can arise from hierarchical differences in synaptic properties, including excitatory strengths. In turn, models have shown how hierarchical differences in synaptic properties can contribute to functional specialization of areas, such as their capacity to generate robust persistent activity related to working memory computations (Chaudhuri et al., 2015; Murray et al., 2017).

fMRI has also revealed functional organization of human cortex along sensory-association hierarchical gradients. Margulies et al. (2016) found that the principal gradient of rs-FC variation across cortex separated primary sensory areas from higher-order association areas, and this gradient aligns with the topography of intra-cortical myelin content as measured by T1 mapping (Huntenburg et al., 2017). Compared to sensory cortex, association areas exhibit greater variation in rs-FC profiles across subjects, suggesting that cortical hierarchy plays a role in shaping single-subject specificity of FC patterns (Mueller et al., 2013; Finn et al., 2015). Our model provides a circuit mechanism linking hierarchical variation in microcircuit properties to functional specialization.

Relationships between dMRI-derived SC and rs-FC in human cortex have been consistently shown in prior studies (Greicius et al., 2009; Hagmann et al., 2008; Honey et al., 2009; Baria et al., 2013) and provide the foundation for large-scale structure-function relationships. Computational studies of large-scale cortical circuits have shown that the structure-function relationship improves when neural dynamics are near the edge of instability (Deco et al., 2013, 2014), which was also confirmed in our study. Here, we showed that heterogeneity in local microcircuit properties has a substantial effect on model FC predictions, beyond prior modeling studies. In addition to the role of SC in shaping FC, this study provides a complementary perspective that emphasizes the importance of intrinsic properties within local circuits in shaping the large-scale functional organization of human cortex.

Beyond the T1w/T2w-based hierarchical heterogeneity map examined here, our model framework can be flexibly extended to include other axes of variation. Heterogeneity maps could reflect varying distributions of receptor subtypes, neuronal cell types, and neuromodulators. These maps could be derived from gene expression, positron emission tomography, or autoradiography. Large-scale models can be fit to pharmacological neuroimaging, through simulation of hypothesized parameter perturbations that follow the expression topography of affected receptors (Preller et al., 2018; Murray et al., 2018). This approach can further be applied to clinical neuro-imaging to fit the heterogeneous effects of disorder-related alterations (Yang et al., 2016; Murray et al., 2018). Further computational studies of areal heterogeneity can further inform the relationships among structure, function, and physiology in the human brain.

An important limitation in modeling neural mechanisms underlying rs-FC is the existence of multiple, potentially confounding, non-neural contributions to noninvasive neuroimaging measures, such as head motion, respiration, and heart-rate variability (Power et al., 2017). Individual differences in non-neural measures did not explain the improvement in model-empirical FC fit by the heterogeneous model. Nevertheless, complete removal of, or control for, non-neural confounds in a given neuroimaging modality is difficult. Characterization of neural sources of rs-FC components can be provided through convergence of multiple

modalities (Kucyi et al., 2018), including invasive recordings in animal models (Schölvinck et al., 2010; Mateo et al., 2017).

Our heterogeneous circuit model is parsimonious, as it simulates simplified local node dynamics, comprises only cortex, and implements a single neural axis of microcircuit specialization. The model framework can be extended in multiple important directions, which will expand the range of questions it can address. More complex local node models with multiple neurobiological dynamical processes, and inclusion of subcortical structures, may be needed to capture frequency-specific features of FC and power spectra (Keitel and Gross, 2016; Mellem et al., 2017; Frauscher et al., 2018; Salvador et al., 2005). For instance, cortical microcircuitry exhibits hierarchical gradients in the densities of multiple classes of inhibitory interneurons (Burt et al., 2018). An extended cortical microcircuit model with distinct superficial and deep layers could exhibit richer spectral features (Mejias et al., 2016). Such greater diversity of temporal dynamics likely cannot be resolved by fMRI but can potentially be constrained by MEG, electroencephalography (EEG), or electrocorticography (ECoG). Multimodal functional neuroimaging may play a key role in the development of biophysically based circuit models that operate across a wide range of spatiotemporal scales.

Another promising direction for model extension is to incorporate subcortical structures, which can be generators of distinct dynamical processes. For instance, our cortical model does not capture strong alpha-band power in occipital cortex, which is thought to originate from interactions between cortex and thalamus (Hughes and Crunelli, 2005). Dynamical neural models of a thalamocortical loop can capture key aspects of resting-state dynamics, such as dynamics of alpha-band activity in occipital cortex measured with EEG (Freyer et al., 2011). This circuit modeling framework is well suited to study how large-scale recurrent cortico-subcortical interactions shape the spatiotemporal dynamics of cortex.

In conclusion, we report a large-scale neural circuit model of human cortex with hierarchical heterogeneity of local microcircuit properties across cortical areas. The model proposes a specific circuit mechanism for how microcircuit specialization shapes the large-scale functional organization of human cortical dynamics. Our findings highlight the importance of regional heterogeneity in local circuit properties and provide support for a hierarchical neural axis reflecting important structure-function relationships in the human brain.

STAR☆METHODS

Detailed methods are provided in the online version of this paper and include the following:

CONTACT FOR REAGENT AND RESOURCE SHARING

Further information and requests for resources and reagents should be directed to and will be fulfilled by Lead Contact, John D. Murray (john.murray@yale.edu).

EXPERIMENTAL MODEL AND SUBJECT DETAILS

Multi-modal Neuroimaging Dataset—We used resting-state fMRI (rs-fMRI) and diffusion MRI (dMRI) of 334 unrelated subjects from the Human Connectome Project

(HCP) 900-subject data release (12/08/2015) (Van Essen et al., 2013). The magnetic resonance (MR) preprocessing relied on the surface-based multimodal intersubject registration (MSMAll) (Robinson et al., 2014). The analyses also involved resting-state magnetoencephalography (MEG) data of 89 subjects from the same HCP dataset.

Cortical areas were defined according to a multimodal parcellation (MMP1.0) comprising 360 areas, 180 per hemisphere, using the 210P boundaries from Glasser et al. (2016). Intersubject alignment in the HCP dataset was achieved using multi-modal areal-feature-based surface registration (MSMAll) (Robinson et al., 2014), which provides a number of improvements over registration techniques based only on geometrical features (such as cortical folding) and reduces biases due to registration error in group-averaged datasets. Cortical parcel boundaries in this parcellation were defined using convergent data features from multiple independent magnetic resonance imaging modalities, including T1w/T2w, cortical thickness, task-based fMRI, and resting-state functional connectivity gradients. The MMP1.0 parcellation was defined using the same HCP dataset used in our present study.

METHOD DETAILS

Resting-State Functional Connectivity—The preprocessing of rs-fMRI time series was done according to the HCP minimal preprocessing pipeline; for details see Glasser et al. (2013). BOLD time series were further denoised using ICA-FIX which yielded the signal that drove the cortical parcellation used in this study (Glasser et al., 2016). ICA-FIX is designed to remove spatially structured artifactual signals through application of independent component analysis (ICA), and a machine-learning algorithm applied to classify structured components into signal or artifact. Artifactual components are then regressed out of the data, yielding a de-noised signal. No further preprocessing step was performed to ensure that the time series are consistent with those that produced the parcellations as referenced in Glasser et al. (2016). We note that other pre-processing methods are available, but not investigated here, such as regression based on physiological measurements (Kasper et al., 2017).

The rs-fMRI time series of each subject comprised 4 sessions each spanning 15 min recorded with repetition time (TR) 0.72 s. The rs-fMRI time series were parcellated into 360 areas (180 areas per hemisphere) using the MMP1.0 parcellation (Glasser et al., 2016). We removed the first 100 time points from each of the BOLD scans to mitigate any baseline offsets or signal intensity variation. We z-scored the time series of each area, then parcellated time series of each subject were concatenated to a single time series comprising 4,400 time points (52.8 min). The time series of each area was z-scored again after concatenation. The functional connectivity (FC) matrix of each subject was computed using Pearson's correlation coefficient between the time series of all pairs of areas.

Structural Connectivity—Structural connectivity (SC) matrices were constructed using probabilistic tractography, for each of the 334 subjects, from the HCP diffusion MRI (dMRI) minimally preprocessed data (Glasser et al., 2013; Sotiropoulos et al., 2013). Following the HCP dMRI step, the diffusion images underwent FSL's bedpostx and probtrackx2 analysis workflows for probabilistic tractography. The SC matrices were derived by seeding at the

white matter-gray matter boundary interface and counting the number of streamlines that intersected 60,000 white matter-gray matter boundary locations. Fiber orientations used in tractography were derived using a parametric deconvolution approach available in FSL (Jbabdi et al., 2012; Hernández et al., 2013; Sotiropoulos et al., 2016) (up to 3 orientations per voxel).

The dense connectome was then parcellated by considering the average between pairs of areas, and the resulting SC matrices were averaged across subjects. The diagonal elements of the group-averaged SC matrix were removed and then values of the SC were normalized between 0 and 1 (i.e., the SC matrix was divided by the maximum SC weight). For use in the computational model, the SC matrix was normalized row-wise, so that the summed long-range input strengths are equalized for each node in the network, which is simulated as a cortical microcircuit. Due to row-wise normalization, the net SC in-degree does not vary across nodes in the models.

T1w/T2w maps—The MSMAll registered and bias field-corrected maps of the ratio between T1- to T2-weighted images (T1w/T2w) were provided with the HCP dataset. In the MMP parcellation, each of the 180 areas in each hemisphere is assigned a paired homolog in the other hemisphere (Glasser et al., 2016). For homologous parcels between left and right hemispheres to have the same hierarchical level in the heterogenous model, the T1w/T2w maps were symmetrized by averaging the T1w/T2w map values of the homologous parcels between left and right hemispheres.

MEG Data Processing—We used eyes-open resting-state MEG data of 89 subjects from the Human Connectome Project (HCP) (Larson-Prior et al., 2013; Van Essen et al., 2013). 3 runs of 6 min each were recorded per subject with a sampling frequency of 2034.5 Hz. Preprocessing included in the HCP release performed the following steps: removal of channels and segments as determined by the HCP quality assurance standards (Larson-Prior et al., 2013), bandpass (1.3–150 Hz) and notch (59–61 Hz, 119–121 Hz) filtering, and removal of non-brain components through ICA. A precomputed single shell volume conduction model was provided in this HCP release.

Preprocessing followed the pipeline provided in the HCP dataset (Larson-Prior et al., 2013; Van Essen et al., 2013), the steps of which we summarize here. Source reconstruction was performed for approximately 8,000 vertices on the cortical surface, using the software provided by HCP and custom scripts written in MATLAB and employing the FieldTrip toolbox. Sensor data were bandpass filtered from 1.3 to 55 Hz and then projected to source space by synthetic aperture magnetometry. The sensor-covariance matrix was regularized by adding a value of 75% of its mean eigenvalue to the diagonal, and the noise covariance was assumed spherical. The direction of the source dipole was determined using a non-linear search in each dipole's tangential plane to obtain the maximum signal-to-noise-ratio for the source power. After source reconstruction on the 8k-grid, source time courses were parcellated using the 360-area MSMAll atlas. Each parcel's time course was determined as the first principal component of its constituting voxels' time courses, and then z-scored. We note that the spatial resolution of source-reconstructed MEG signals is lower than that of

fMRI (Larson-Prior et al., 2013), which is likely to degrade the regional specificity of MEG spectral features.

The power spectral density (PSD) for each parcel was computed using Welch's method with a frequency resolution of about 1 Hz. For each parcel, the PSDs were averaged across subjects and runs, and then normalized such that the integrated PSD over the range 3–50 Hz equals 1. Analyses were performed on these cortical relative power maps, as in prior studies (Mellem et al., 2017; Hillebrand et al., 2012; Martín-Buro et al., 2016). The relative power map, defined for a particular frequency or band, provides a regional topography of the relative contribution of that frequency to the region's power.

However, the presence of a strong peak in the alpha-frequency range — and to a lesser degree in the beta-range — for some, but not all, parcels strongly affects the normalization factor. As a result, the information about the alpha (and beta) peak impacts the relative power maps of other frequencies through the normalization. We therefore sought to analyze relative power with these peaks removed prior to normalization. To remove alpha and beta peaks, we first fit the group-averaged PSDs with models with sums of Lorentzian distributions (Chaudhuri et al., 2018). Specifically, we fit the following two models individually to each parcel's group-averaged PSD:

$$p_\alpha(f) = L(a_1, 0, \gamma_1, f) + L(a_2, c_2, \gamma_2, f) =: L_0 + L_\alpha \quad (1)$$

with free parameters a_1; γ_1; a_2; c_2; γ_2 and

$$p_{\alpha\beta}(f) = L(a_1, 0, \gamma_1, f) + L(a_2, c_2, \gamma_2, f) + L(a_3, c_3, \gamma_3, f) =: L_0 + L_\alpha + L_\beta \quad (2)$$

with free parameters $a_1; \gamma_1; a_2; c_2; \gamma_2; a_3; c_3; \gamma_3$. Here,

$$L(a, c, \gamma, f) = \frac{a}{1 + \left(\frac{f - c}{\gamma}\right)^2} \quad (3)$$

is a Lorentzian distribution over frequency f defined by amplitude a, center frequency c and half-width γ. Fitting was performed using least-squares with the following constraints on the parameters : $a_1 \in [0, a_m]$, $\gamma_1 \in [1,15]$, $a_2 \in [0, a_m]$, $c_2 \in [7,15]$, $\gamma_2 \in [1,15]$, $a_3 \in [0, a_m]$, $c_3 \in [15.1,30]$ and, $\gamma_3 \in [1,15]$, where is the bound a_m is 1.5 times the maximal amplitude in the parcel's empirical power spectrum. The best fit obtained from 10 random initializations was used. We then subtracted L_a and L_β from the parcel's empirical group-averaged PSD, and then normalized it such that it sums to 1. According to both the R^2 goodness-of-fit metric and visual inspection, the $p_{a\beta}$ fit provided a cleaner removal of the peaks in the PSD than the p_a fit, and we therefore preferred $p_{a\beta}$ (Figure S8).

Resting-State Network Assignments—We used network-level analyses to characterize the hierarchical organization of empirical and simulated resting-state FC measure (i.e.,

comparison of the variation between sensory versus association areas). Resting-state network (RSN) assignment was performed through community detection analysis on the correlation between resting-state fMRI time series of the HCP dataset (Ito et al., 2017). This network assignment was selected because it was performed on the MMP1.0 parcellation and the HCP dataset used here, and because it yielded networks with sufficient granularity for comparisons between sensory and association networks. Specifically, this approach yielded 8 functional networks in cortex, which corresponded to functional networks identified elsewhere in the literature: three sensory networks (visual, auditory, and somatomotor), and five association networks (dorsal attention, ventral attention, default mode, fronto-parietal and cingulo-opercular). The sensory-association comparisons were performed by combining the values across the three sensory networks, and across the five association networks.

Large-Scale Computational Model

Synaptic Dynamical Equations: We adapted the biophysically-based large-scale computational model proposed by Deco et al. (2014). This model reduces the complexity and the number of local microcircuit parameters in a spiking neural network model using a dynamical mean field approach (Wong and Wang, 2006). Exploiting the long time-constants of NMDA receptors, the local node model reduces from a large spiking neural network to a two-dimensional dynamical system.

Each cortical area is characterized by a microcircuit comprising a system of coupled excitatory and inhibitory populations. For each cortical microcircuit node $i \in \{1, \ldots, N\}$, excitatory (E) and inhibitory (I) currents are given by:

$$I_i^E(t) = W^E I_b + w^{EE} S_i^E(t) + gJ \sum_j C_{ij} S_j^E - w^{IE} S_i^I(t) \quad (4)$$

$$I_i^I(t) = W^I I_b + w^{EI} S_i^E(t) - S_i^I(t) \quad (5)$$

where $W^p I_b$ and S_i^p, respectively, denote the background current and synaptic gating variable for each population $p \in \{E, I\}$ g is the global coupling parameter, C_{ij} is the long-range structural connectivity strength from node j to node i, J is the effective NMDA conductance, W^{EE} sets the local excitatory-to-excitatory strength, W^{EI} sets the local excitatory-to-inhibitory strength, and W^{IE} sets the local inhibitory-to-excitatory strength.

The firing rate of each population, r^p, $p \in \{E, I\}$ is computed using the transfer function $\phi(I_i^p)$:

$$r_i^p(t) = \phi(I_i^p(t)) = \frac{a^p I_i^p(t) - b^p}{1 - e^{-d^p(a^p I_i^p(t) - b^p)}} \quad (6)$$

Finally, the synaptic gating variables obey:

$$\frac{dS_i^E(t)}{dt} = -\frac{S_i^E(t)}{\tau_E} + \left(1 - S_i^E(t)\right)\gamma r_i^E(t) + \sigma v_i(t) \quad (7)$$

$$\frac{dS_i^I(t)}{dt} = -\frac{S_i^I(t)}{\tau_I} + r_i^I(t) + \sigma v_i(t) \quad (8)$$

where σ is the standard deviation of the input noise taken from a random Gaussian process n_i (Wong and Wang, 2006; Deco et al., 2014).

Implementing feedback inhibition control (FIC) proposed in Deco et al. (2014), for each parameter set, the inhibitory-to-excitatory strengths W^{IE} were adjusted to satisfy the condition $r_i^E \approx 3$ Hz. This was done by analytically solving for W^{IE} to satisfy the self-consistency of Equations 4–8 at the steady-state condition with $r_i^E \approx 3$ Hz, which corresponds to $\langle S^E \rangle \approx 0.164757$ and $\langle I^E \rangle \approx 0.37738$ nA:

$$w_i^{IE} = \frac{W^E I_b + w^{EE}\langle S^E \rangle + gJ\langle S^E \rangle - \langle I^E \rangle}{\langle S^I \rangle} \quad (9)$$

where the steady-state inhibitory synaptic gating variable $\langle S_i^I \rangle = \phi\left(\langle I_i^I \rangle\right)\tau_I$ was estimated numerically by solving for $\langle I_i^I \rangle$:

$$W_i^I I_b + w^{EI}\langle S^E \rangle - \phi\left(\langle I_i^I \rangle\right)\tau_I - \langle I_i^I \rangle = 0 \quad (10)$$

Hemodynamic Equations: The synaptic activity of each cortical area is defined by the excitatory synaptic gating variable ($\mathbf{S^E}$). The excitatory synaptic activity of each area was transformed to a blood-oxygen-level dependent (BOLD) signal using the Balloon-Windkessel model (Friston et al., 2003). The three dimensionless magnetic field strength-dependent parameter values k_1, k_2, and k_3 were derived for 3T using Appendix A of Heinzle et al. (2016); all other hemodynamic parameter values were taken from Obata et al. (2004). In the Balloon-Windkessel model, the hemodynamic response obeys the following system of equations:

$$\frac{dx(t)}{dt} = S^E(t) - kx(t) - \gamma(f(t) - 1) \quad (11)$$

$$\frac{df(t)}{dt} = x(t) \quad (12)$$

$$\tau\frac{dv(t)}{dt} = f(t) - v^{\frac{1}{\alpha}}(t) \quad (13)$$

$$\tau\frac{dq(t)}{dt} = \frac{f(t)}{\rho}\left[1 - \left((1-\rho)^{\frac{1}{f(t)}}\right)\right] - q\left(v^{\frac{1}{\alpha}-1}(t)\right) \quad (14)$$

where S^E is the excitatory synaptic gating variable, x is the vasodilatory signal, f is blood inflow, v is blood volume, and q is deoxyhemoglobin content; parameters ρ, τ, κ, λ, and α are the resting oxygen extraction fraction, hemodynamic transit time, rate of signal decay, rate of flow-dependent elimination, and the Grubb's exponent, respectively. The BOLD signal is then calculated as

$$y(t) = V_0\left[k_1(1-q(t)) + k_2\left(1 - \frac{q(t)}{v(t)}\right) + k_3(1-v(t))\right] \quad (15)$$

where V_0 is the resting blood volume fraction.

Values for all fixed parameters in Equations 4–15 are provided in Table 1.

Analytical Approximation of BOLD Functional Connectivity: Correlations between the excitatory population activity of the modeled cortical microcircuits can be approximated analytically by linearizing the system near a stable fixed point Deco et al. (2013, 2014). In brief, the linearization of the model equations enables computationally efficient calculation of the synaptic FC matrix. However, in prior studies by Deco et al. (2013, 2014), this calculation was not extended to fluctuations of the BOLD signal. We extended the linearization approximation to include the hemodynamic model for the BOLD signal. The computational efficiency provided by analytical calculation of the BOLD FC matrix was required for computationally tractable fitting of model parameters to empirical BOLD FC data.

The details of the derivation for the statistical moments of the synaptic equations were described previously in Deco et al. (2013, 2014). Here, we combine the equations that describe synaptic dynamics (Equations 7–8) and the hemodynamic response (Equations 11–14) to form a single dynamical system comprised of two synaptic and four hemodynamic state variables. Given the Jacobian matrix A and noise covariance matrix Q_n of the extended system, evaluated at the system's stable fixed point, the covariance matrix P can be approximated analytically by solving the Lyapunov equation:

$$AP + PA^T + Q_n = 0 \quad (16)$$

The Jacobian of the extended system is determined by the partial derivatives of the equations for synaptic dynamics (Equations 7 and 8) and the hemodynamic response (Equations 11–14). The synaptic sub-block of the full Jacobian matrix is obtained by expanding the synaptic equations (Equations 7 and 8) around the synaptic variables' stable fixed point:

$$\frac{\partial \dot{S}_i^E}{\partial S_i^E} = -\frac{1}{\tau_E} + \left(1 - \langle S_i^E \rangle\right) \gamma \frac{\partial \phi_i^E \left(\langle I_i^E \rangle\right)}{\partial S_i^E} w_i^{EE} - \gamma \phi_i^E \left(\langle I_i^E \rangle\right) \quad (17)$$

$$\frac{\partial \dot{S}_i^E}{\partial S_j^E} = \left(1 - \langle S_i^E \rangle\right) \gamma \frac{\partial \phi_i^E \left(\langle I_i^E \rangle\right)}{\partial S_j^E} \frac{1}{\sum_j C_{ij}} gJC_{ij}, \ i \neq j \quad (18)$$

$$\frac{\partial \dot{S}_i^E}{\partial S_i^I} = -\left(1 - \langle S_i^E \rangle\right) \gamma \frac{\partial \phi_i^E \left(\langle I_i^E \rangle\right)}{\partial S_i^I} w_i^{IE} \quad (19)$$

$$\frac{\partial \dot{S}_i^I}{\partial S_i^E} = -\partial \frac{\phi_i^I \left(\langle I_i^I \rangle\right)}{\partial S_i^E} w_i^{EI} \quad (20)$$

$$\frac{\partial \dot{S}_i^I}{\partial S_i^I} = -\frac{1}{\tau_I} - \frac{\partial \phi_i^I \left(\langle I_i^I \rangle\right)}{\partial S_i^I} \quad (21)$$

$$\frac{\partial \dot{S}_i^E}{\partial S_j^I} = \frac{\partial \dot{S}_i^I}{\partial S_j^I} = 0 \quad (22)$$

where $\langle \dots \rangle$ denotes the temporal average (i.e., the steady-state value). The remaining non-zero elements of the full Jacobian matrix A can then be obtained by computing the partial derivatives of hemodynamic equations (Equations 11–14) with respect to the four hemodynamic variables and the excitatory synaptic gating variable, given by:

$$\frac{\partial \dot{x}_i}{\partial S_j^E} = \delta_{ij} \quad (23)$$

$$\frac{\partial \dot{x}_i}{\partial x_j} = -\kappa \delta_{ij} \quad (24)$$

$$\frac{\partial \dot{x}_i}{\partial f_j} = -\gamma \delta_{ij} \quad (25)$$

$$\frac{\partial \dot{f}_i}{\partial x_j} = \delta_{ij} \quad (26)$$

$$\frac{\partial \dot{v}_i}{\partial f_j} = \frac{1}{\tau} \delta_{ij} \quad (27)$$

$$\frac{\partial \dot{v}_i}{\partial v_j} = -\frac{1}{\tau \alpha} \delta_{ij} \quad (28)$$

$$\frac{\partial \dot{q}_i}{\partial f_j} = \frac{1}{\tau} \left[1 + \frac{1}{\rho}(1 - \rho)\ln(1 - \rho) \right] \delta_{ij} \quad (29)$$

$$\frac{\partial \dot{q}_i}{\partial v_j} = \frac{\alpha - 1}{\alpha \tau} \delta_{ij} \quad (30)$$

$$\frac{\partial \dot{q}_i}{\partial q_j} = -\frac{1}{\tau} \delta_{ij} \quad (31)$$

where δ_{ij} if $i \neq j$, and δ_{ij} otherwise. All other partial derivatives are identically 0. From the full Jacobian A, the covariance matrix of the extended system P is then estimated by solving the Lyapunov equation (Equation 16). Finally, the covariance matrix of the first-order BOLD signal fluctuations is given by:

$$P^{BOLD} = KPK^{\dagger} \quad \# \quad (32)$$

where K is the matrix of partial derivates of the BOLD signal (Equation 15), evaluated at the fixed point. The model-estimated BOLD FC matrix can then be computed from the BOLD covariance matrix $\mathbf{P}^{BOLD}$ via

$$FC_{ij}^{BOLD} = \frac{P_{ij}^{BOLD}}{\sqrt{P_i^{BOLD}P_j^{BOLD}}}. \quad (33)$$

The parameters for estimating the BOLD signal were updated based on Heinzle et al. (2016), to match the parameters used for 3T field strength (i.e., $k_1 = 3.72$, $k_2 = 0.53$, $k_3 = 0.53$).

The transformation of the synaptic signals to BOLD signals may operate in part as a low-pass filter. We observed that the analytical BOLD FC was highly correlated with the low-frequency coherence in the synaptic system. To further characterize the role of BOLD linearization on the model fit performance, we compared the analytical BOLD FC and synaptic FC. For the homogeneous model, the similarity between synaptic and BOLD FC was high ($r = 0.99 \pm 0.002$). In contrast, the heterogeneous model BOLD FC exhibited lower similarity to the synaptic FC (average $r = 0.955 \pm 0.005$, worst $r = 0.90$). Furthermore, the magnitudes of the correlations in synaptic FC were substantially lower than the correlations in BOLD FC. Therefore, simulation of hemodynamics might have substantial impact on a model's fit to empirical BOLD FC (Figure S3).

Theoretical Characterization of the Model—To provide a mechanistic view of the local microcircuit dynamics, we performed theoretical analysis of the model from a dynamical systems approach. We first characterized the dynamical stability and the qualitative behavior of a single model node, with no external current ($I_{ext} = 0$). For a set of local excitatory-to-excitatory and excitatory-to-inhibitory synaptic strengths (W^{EE} and W^{EI}, respectively), the feedback inhibitory-to-excitatory strength W^{IE} is set to maintain an excitatory firing rate at $r^E \approx 3$ Hz (Deco et al., 2014) (See section: Homogeneous and heterogeneous modeling paradigms). Therefore, although the phase diagram was constructed for W^{EE} and W^{EI}, the solution of the system implicitly depends on W^{IE}.

The stability of the model was characterized by the largest eigenvalue λ of the Jacobian matrix A of the synaptic system. We denote $\Re\{\lambda\}$ and $\Im\{\lambda\}$ as the real and imaginary parts, respectively, of the eigenvalue with largest real part. The fixed point dynamics are stable if $\Re\{\lambda\} < 0$ and $\Im\{\lambda\} = 0$, unstable if $\Re\{\lambda\} > 0$ and $\Im\{\lambda\} = 0$, stable spiral if $\Re\{\lambda\} < 0$ and

$\mathfrak{J}\{\lambda\} \neq 0$, and unstable spiral if $\mathfrak{R}\{\lambda\} > 0$ and $\mathfrak{J}\{\lambda\} \neq 0$ The system exhibits a pitchfork bifurcation when $\mathfrak{J}\{\lambda\} = 0$ and a Hopf bifurcation when $\mathfrak{J}\{\lambda\} \neq 0$.

For W^{EI} values between 0.001 and 5, we numerically solved the equations for W^{EE} when $\mathfrak{R}\{\lambda\} = 0$ and $\mathfrak{J}\{\lambda\} = 0$ to determine critical points. The natural frequency of the system was calculated as $|\mathfrak{J}\{\lambda\}|/2\pi$.

To illustrate optimal model parameters projected onto the phase plane, we adjusted the external input according to the total synaptic input to each area such that $I_{ext} = gJ\langle S^E \rangle$ where g the global coupling parameter and J is the long-range NMDA conductance, and $\langle S^E \rangle$ is the average synaptic gating variable.

To characterize modes of spatiotemporal dynamics in the fully connected models, we performed eigenvalue and eigenvector analyses on the heterogeneous and homogeneous models at the optimal solutions. We performed eigen-decomposition of the Jacobian matrix and then we ordered the eigenvalues by characteristic timescale (i.e., $-1/\mathfrak{R}\{\lambda\}$). Then we studied the patterns of the corresponding eigenvectors of the system. In particular, we examined the relationship between the eigenvector of the slowest mode and the T1w/T2w-based hierarchical heterogeneity map (Figure S6).

Homogeneous and Heterogeneous Modeling Paradigms—In both modeling paradigms, all parameters were kept constant except local excitatory-to-excitatory synaptic strength W^{EE}, excitatory-to-inhibitory synaptic strength W^{EI}, and global coupling parameter g. In the homogeneous model, the values of recurrent excitatory synaptic strength W^{EE} and excitatory-to-inhibitory synaptic strength W^{EI} were assigned globally; i.e., the same value for each area. In the heterogeneous model, W^{EE} and W^{EI} were defined by a map based on the hierarchical level of each area.

We showed that the T1w/T2w map is characterized by high values in sensory regions and low values in association regions (Figure 1). In the heterogeneous model, we introduced hierarchical heterogeneity using the median T1w/T2w map values computed across 334 subjects. The raw T1w/T2w map values across brain areas exhibit a positively skewed distribution (Glasser et al., 2014). For model parameterization, we transformed the raw T1w/T2w map values into hierarchical heterogeneity map values which are more uniformly distributed, rescaled between 0 and 1, and inverted such that high- (low-) T1w/T2w areas have low (high) hierarchical heterogeneity map values (Figure S2). Specifically, hierarchical heterogeneity map value h_i, for each i, was determined by:

$$h_i = \frac{\max\{T\} - T_i}{\max\{T\} - \min\{T\}} \quad (34)$$

T_i is calculated from the raw T1w/T2w value $\left(T_i^{(raw)}\right)$ using the error function erf: $T_i = \text{erf}\left(T_i^{(raw)}\right)$. Local microcircuit parameters W^{EE} and W^{EI} were linearly scaled by h_i map values:

$$w_i^{EE} = W_{\min}^{EE} + W_{\text{scale}}^{EE} h_i \quad (35)$$

$$w_i^{EI} = w_{\min}^{EI} + w_{\text{scale}}^{EI} h_i \quad (36)$$

where the subscript min denotes the minimum parameter value and the subscript "scale" denotes the scaling factor that defines the steepness of the hierarchical heterogeneity map. We note that the above procedure for setting local parameters as a function of the T1w/T2w values is only one possible implementation. In particular, monotonic but nonlinear transformations could provide higher-order dependencies, but these were not investigated in this study.

Because the sensory–association distinction is a prominent feature of the T1w/T2w map, we tested an alternative heterogeneity map reflecting only the binary categorization of areas into sensory versus association networks. Specifically, we fit the model using a heterogeneity map parameterized such that W_{EE} and W_{EI} strengths can each take only two values, one within sensory networks (visual, somatomotor, auditory) and another within association networks. The resulting map is assigned a value of 0 for all areas assigned to sensory networks, and a value of 1 for other areas.

We used white-matter/gray-matter seeding for diffusion tractography, as this improves agreement of within-hemisphere connectivity with tracer-measured connection strengths (Donahue et al., 2016). We focused on modeling and analyzing within each hemisphere, i.e., not including inter-hemispheric connections, for multiple reasons. First, this focus prioritized fitting the network structure of FC, rather than inter-hemispheric FC of homologous areas. Second, dMRI tractography may have relatively poorer performance at mapping callosal connections. Consistent with this consideration, the correlation between SC and FC in the HCP dataset is higher for intra-hemispheric connections (Figure S1). Third, this focus selection increased computational efficiency of model fitting, as on our high-performance computing cluster, the runtime of a single execution of the model was approximately 1 s for the intra-hemispheric model (180 regions), whereas it exceeded 10 s for the entire cortex (360 regions). For these reasons, we excluded inter-hemispheric connections and simulated the left and right hemisphere models separately. In both homogeneous and heterogeneous paradigms, the models comprised two intra-hemispheric compartments in which the local microcircuit parameters in homologous areas are identical but the two hemispheres do not interact.

Optimization of Model Parameters—We estimated the optimal model parameters for homogeneous and heterogeneous models. The homogeneous model included four free parameters: W^{EE}, W^{EI}, and g_I, and g_r. The heterogeneous model parameters included six free parameters: W_{min}^{EE}, W_{scale}^{EE}, W_{min}^{EI}, W_{scale}^{EI}, and g_I, and g_r.

Bayesian statistics has substantial advantages over point estimates of model parameters because it provides a better description by estimating the full posterior probability distributions of the model parameters. However, estimation of the model FC is based on a stochastic dynamical system. Therefore, it is not possible to analytically solve for the likelihood function. For this reason, we used Approximate Bayesian Computation (ABC), which approximates the likelihood function by minimizing a distance measure, to estimate the optimal model parameters. To find the model parameters that minimize the distance between empirical FC (FC) and model FC ($\widehat{FC}$) we used adaptive hierarchical Population Monte Carlo (hPMC) (Beaumont et al., 2009; Turner and Van Zandt 2014). Since the variations across subjects are removed in average FC, we defined the distance measure based on individual FCs. Specifically, we estimated parameters which minimized the average empirical to model FC distance across the entire population (Turner and Van Zandt, 2014) (Figures S2 and S4).

In the initial step, each parameter value was drawn from its prior distribution (Table 2). In subsequent steps, the parameters were drawn from a proposal distribution. The prior distributions were informed by the phase-diagram (Figures 6 and S6).

In the PMC approach, a particle is defined as a set of model parameters that is drawn from the proposal distribution. For each particle, the model FC ($\widehat{FC}$) was calculated according to Equation 32, if the system of equations is dynamically stable. Then, we calculated the distance (δ) as:

$$\delta = 1 - \left(\frac{1}{S} \sum_i^S r^{FC_i, \widehat{FC}} - \left(\left| \left\langle \frac{1}{S} \sum_i^S FC_i \right\rangle - \left\langle \widehat{FC} \right\rangle \right| \right)^2 \right) \quad (37)$$

where r is the Pearson correlation coefficient, $S \in \{1, \ldots, 334\}$ is the number of subjects, and $\langle\rangle$ denotes the average FC across regions. first term in the parentheses of Equation 37 quantifies the average Pearson distance between the model FC and subject FCs. The second term is an additional cost term quantifying the difference between mean FCs (since Pearson correlations involve mean-subtraction), ensuring that the mean model FCs do not diverge from the mean empirical FCs.

The particles were rejected if the distance, δ, was larger than the rejection threshold ε. Initially, the rejection threshold was defined as the Pearson correlation distance between the empirical FC and SC. In subsequent iterations, the rejection threshold was iteratively adjusted according to the first quantile of accepted distances in the previous iteration. The algorithm was run until the number of accepted particles exceeded the minimum sample size (N). For the rest of the iterations (T), samples were drawn from the proposal distribution:

$$\hat{\pi}_t\left(\theta^{(t)}\right) \propto \sum_{j=1}^N w_j^{(t-1)} K_t\left(\theta^{(t)} \middle| \theta_j^{(t-1)}\right) \quad (38)$$

where the importance weight W_i^t for an accepted particle θ_i^t is

$$w_i^t \propto \frac{\pi\left(\theta_i^{(t)}\right)}{\hat{\pi}_t\left(\theta_i^{(t)}\right)} \quad (39)$$

and the random walk kernel (K_t) is defined as:

$$K_t\left(\theta^{(t)} \middle| \theta_j^{(t-1)}\right) = \tau^{-1}\varphi\left\{\tau^{-1}\theta^{(t)} - \theta_j^{(t-1)}\right\} \quad (40)$$

where φ is standardized (multivariate) normal density and τ is the scaling factor, which is calculated as twice the weighted empirical covariance: $\tau^2 = 2\text{Cov}(\theta)$.

In both homogeneous and heterogeneous models, the minimum sample size was set to $N = 1000$ and the maximum number of iterations was set to $T = 100$. The algorithm was terminated if it reached either the maximum number of iterations or the acceptance rate (i.e., N/N_{total}) was lower than 0.001, indicating convergence. The homogeneous model converged after 74 iterations and the heterogeneous model converged after 84 iterations due to low acceptance rate, but the distance between empirical and model FC stabilized after approximately 50 iterations (Figure S4).

To test that the improved fitting in the heterogeneous model is not due to overfitting with the higher number of degrees of freedom in the model, we performed leave-p-out cross-validation. We repeated the optimization procedure for both homogeneous and heterogeneous models (using left cortical hemisphere, minimum sample size $N = 200$, maximum number of iterations $T = 50$) on 267 of 334 subjects, after holding out 20% of the subjects randomly (non-overlapping subjects). Then, we calculated the model fit on the held-out test subjects.

In addition to leave-p-out cross-validation, we compared the T1w/T2w-based hierarchical heterogeneity map against surrogate maps with spatial autocorrelation structure matched to the hierarchical heterogeneity map, as described in the following section (Figure 2). We repeated the procedure for 500 surrogate heterogeneity maps. For computational efficiency, we ran the optimization for left cortical hemisphere, with a minimum of 500 particles for at most 50 iterations.

We also performed this fitting procedure for T1w/T2w map-derived hierarchical heterogeneity maps under the same conditions. The best fit for re-optimized T1w/T2w-based hierarchical heterogeneity maps was the same as that for the main optimization of the heterogeneous model (i.e., left-right concatenated). For all maps, we ensured that the similarity between empirical and model FC stabilized within 50 maximum iterations (Figure S4).

To assess how well the optimization procedure can identify known parameter values, we generated 334 model FC matrices (i.e., the number of subjects) from the approximated

posterior distribution. We then performed the optimization procedure using these FC matrices. We also repeated this procedure after adding an observation noise with $\mathcal{N}(0, 0.05)$ (approximately matching the noise level in the empirical data). Finally, we calculated the errors in estimated model parameters with respect to the original model parameters. Both with and without observation noise, the model recovered the parameter values with low error.

We assessed an alternative parametrization of the model — i.e., which parameters vary along the heterogeneity map — which does not depend on synaptic weights: the time constants of the excitatory and inhibitory populations, τ_E and τ_I, respectively. Here, we multiplied the parameters τ_E and τ_I by a factor a_E and a_I. The time constants decrease if $a < 1.0$, and increase if $a > 1.0$. To ensure that the fixed-point solution of the system does not change, thereby isolating changes in timescales, we updated the equations such that:

$$\frac{dS_i^E(t)}{dt} = -\frac{S_i^E(t)}{\alpha_E \tau_E} + \frac{1}{\alpha_E}\left(1 - S_i^E(t)\right)\gamma r_i^E(t) + \sigma v_i(t) \quad (41)$$

$$\frac{dS_i^I(t)}{dt} = -\frac{S_i^I(t)}{\alpha_I \tau_I} + \frac{1}{\alpha_I}r_i^I(t) + \sigma v_i(t) \quad (42)$$

The posterior distributions for the parameters were defined as $U(0.8, 1.2)$ for $\tau_{\min}$ and $U(0.0, 1.0)$ for τ_{scale} parameters. The rest of the parameters and optimization procedure were the same as the standard parameterization of synaptic strengths.

Ornstein-Uhlenbeck and Simultaneous Autoregressive Models—Below, we describe two simple non-neural models of simulated BOLD dynamics: the Ornstein-Uhlenbeck (OU) process model, and the simultaneous autoregressive (SAR) model, the latter of which is the discrete time counterpart to the former. Fitting these more phenomenological models can test whether hierarchical heterogeneity of local properties improves the fit to empirical FC patterns, with generality across a broader set of dynamical models.

We generalize these models by introducing hierarchical heterogeneity of self-coupling strengths, denoted w_i for node i, which vary across nodes parametrically by the heterogeneity map values $\{h_i\}$ according to:

$$W_i = W_{\min} + W_{\text{scale}}h_i \quad (43)$$

The heterogeneity parameters $W_{\min}$ and W_{scale} were included in the set of fit parameters for each model.

Ornstein-Uhlenbeck Process Model—We simulated BOLD activity directly with a coupled OU-process model which, when written as a Langevin equation, has the standard functional form, for the activity y_i of node i:

$$\dot{y}_l(t) = -y_i(t) + \sum_j A_{ij} y_j(t) + \sigma v_i(t) \quad (44)$$

where σ sets the strength of noise inputs and $v_i(t)$ is independent Gaussian white noise. For the coupling matrix $\mathbf{A}$, we use the structural connectivity matrix $\mathbf{C}$ scaled by a scalar-valued global coupling parameter G:

$$\dot{y}_l(t) = -\sum_j \left[(1 - w_i)\delta_{ij} - GC_{ij}\right] y_j(t) + \sigma v_i(t) \quad (45)$$

The expression in brackets in Equation 45 above defines the system's Jacobian matrix, i.e.,

$$J_{ij} \equiv -\left[(1 - w_i)\delta_{ij} - GC_{ij}\right] \quad (46)$$

The noise terms, $\sigma v_i(t)$, are assumed to be independent and normally distributed inputs with zero mean and equal variance, as in the dynamic mean-field model, resulting in a noise covariance matrix $\mathbf{Q_n} = \sigma^2 \mathbf{I}$. Thus, we can solve for the covariance matrix of the OU-process model analytically using the Lyapunov equation:

$$JP + PJ^T + Q_n = 0 \quad (47)$$

Simultaneous Autoregressive Model—We simulated BOLD activity directly with a simultaneous autoregressive (SAR) process model. In general, SAR-process models can be written with the temporally discretized functional form

$$\vec{y}_{t+1} = \rho W \vec{y}_t + \epsilon_t, \quad (48)$$

where $\mathbf{W}$ is a weight matrix describing the influence of activity at time t on the activity at time $t+1$, ρ is a coupling constant which scales the strength of this autoregressive process, and ϵ_t is white noise (i.e., serial autocorrelation-free samples with zero mean and finite variance). In general, autoregressive processes are the discrete time analogs of OU processes.

We introduced hierarchical heterogeneity with the addition of a hierarchically varying self-coupling term:

$$y_i^{t+1} = w_i y_i^t + \rho \sum_j C_{ij} y_j^t + \sigma v_i^t \quad (49)$$

where w_i sets the strength of the self-coupling in area i parametrized according to Equation 43, C corresponds to the structural connectivity matrix, and σ sets the standard deviation of the Gaussian noise, i.e., $v_i^t \sim \mathcal{N}(0, 1)$.

To obtain analytic expressions for the covariance matrices, we multiply both sides of Equation 49 by their transposes and apply the temporal averaging operator, $\langle \cdots \rangle$. In the steady-state condition,

$$\left\langle Y_i^{t+1}, Y_j^{t+1} \right\rangle = \left\langle Y_i^t, Y_j^t \right\rangle = Cov(y) \quad (50)$$

from which it follows that

$$Cov(y) = \sigma^2 [(\mathbb{1} - \mathbf{w}) - k\mathbf{C}]^{-1} [(\mathbb{1} - \mathbf{w}) - k\mathbf{C}]^{-T} \quad (51)$$

where **w** is a diagonal matrix.

We fit both OU and SAR models to the empirical BOLD FC using a grid-search algorithm. 20 samples for each parameter (8000 parameter sets in total) were executed from uniform distributions: for OU, $W_{\min}$; W_{scale}; $G = U(0, 1)$; for SAR, $W_{\min} = U(0, 1)$, $W_{\mathrm{scale}} = U(-0.5, 0.5)$, $G = U(0,1)$. The model fit at the optimal solution was $r = 0.517$ for OU, and $r = 0.504$ for SAR. An alternative parametrization of SAR, based on hierarchical heterogeneity of σ_i, produced the same fit value, and therefore was not included here.

Surrogate Heterogeneity Map Generation—First we characterized the spatial autocorrelation structure of median empirical cortical T1w/T2w maps using a spatial lag model. We fit the data using a spatial lag model of the form $\mathbf{y} = \rho \mathbf{Wy}$, where **y** is a vector of first Box-Cox transformed and then mean-subtracted map values. The Box-Cox transformation was first applied to the maps so their values were approximately normally distributed. **W** is the normalized weight matrix with zero diagonal and off-diagonal elements proportional to $W_{ij} = z_i^{-1} \exp(-D_{ij}/d_0)$, where D_{ij} is the surface-based geodesic distance between cortical areas i and j, and $z_i \equiv \Sigma_j \exp(-D_{ij}/d_0)$ is a normalization factor. Weights W_{ij} define the fraction of spatial influence on area i attributable to area j. To calculate j geodesic distances, we used the 32k-vertex midthickness surface mesh in the HCP atlas.

Two free parameters ρ and d_0 are estimated by minimizing the residual sum-of-squares (Anselin, 2001). Using best-fit parameter values $\hat{\rho}$ and $\widehat{d_0}$ surrogate maps $\mathbf{y}_{\mathrm{surr}}$ are generated according to $\mathbf{y}_{\mathrm{surr}} = \left(\mathbb{1} - \hat{\rho}\mathbf{W}[\widehat{d_0}]\right)^{-1}\mathbf{u}$, where $\mathbf{u} \sim \mathcal{N}(0, 1)$ For the Box-Cox normalized T1w/T2w values, this fit yielded $d_0 = 7.00$ mm, and $\rho = 1.060$. To match distributions of

surrogate map values to the distribution of values in the corresponding empirical map (e.g., the T1w/T2w map), rank-ordered surrogate map values were re-assigned the corresponding rank-ordered values in the empirical map. Note that this approach to surrogate data generation approximates a spatial autocorrelation-preserving permutation test of the empirical neuroimaging map.

Using these surrogate maps, we constructed null distributions for $N = 500$ models and report significance values as the proportion of samples in the null distributions whose model fit value is greater than or equal to that obtain from the model using the T1w/T2w-based hierarchical heterogeneity map.

Examination of Potential Confounding Variables—We used regression analysis, performed across subjects, to test whether the improved rs-FC fit of the heterogeneous model, relative to the homogeneous model, may be driven by fitting of FC components attributable to non-neural confounding factors such as head motion, heart rate variations, and respiration (Power et al., 2017). The movement parameters and physiological logs were provided in the HCP dataset. The head motion of each subject was calculated as the mean absolute movement and mean relative movement. Heart rate and respiration variations were calculated as the total variance of each variable across sessions. To test whether the relationship between movement parameters and model fit can explain the improved performance of the heterogeneous model, we constructed a linear regression model ($Y^{(full)}$:

$$Y^{(full)} = \beta_0 + \sum_{k \in C} \beta_k X_k + \text{error} \quad (52)$$

Each subject yields a data point in Y, defined as the difference in model fit for the heterogeneous model compared to the homogeneous model (i.e., $r_{\text{heterogeneous}} - r_{\text{homogeneous}}$). X_k denotes the z-score of four subject-specific non-neural confounding factors k in the set of four denoted C: mean absolute head movement, mean relative head movement, heart rate variance, and respiration variance.

We compared the full regression model $Y^{(full)}$ above to a reduced model that corresponds to the difference in model fit being independent of confounds: $Y^{(reduced)} = \beta_0 + \text{error}$. Through comparison of the full and reduced regression models, we examined the contribution of the non-neuronal confounding factors on the improved model fit in the heterogeneous model. We compared the fraction of variance in the data which is captured by the model, calculating the ratio of explained variance for the full versus reduced regression models, which we found to be very small.

Within-Network and Across-Network Fitting—To study the differences between the performance of the homogeneous and heterogeneous models, we quantified the model fitting for the FCs within and across 8 canonical resting state networks (RSNs). The within-network fit for network N was calculated as:

$$r_N^{within} = r_p\left(\overrightarrow{FC_{lj}^e}, \overrightarrow{FC_{lj}^m}\right), \quad i, j \in N \quad (53)$$

where $\overrightarrow{FC_{lJ}^S}$ $S \in \{e: \text{empirical}, m: \text{model}\}$ is a vector comprising the mean functional connectivity values between regions i and j, and $r_p(x,y)$ denotes the Pearson correlation coefficient between variables x and y. Similarly, the across-network fit for network N is defined as:

$$r_N^{across} = r_p\left(\overrightarrow{FC_{lj}^e}, \overrightarrow{FC_{lj}^m}\right), \quad i \in N \text{ and } j \notin N \quad (54)$$

Global Brain Connectivity—We tested whether hierarchical heterogeneity can also explain rs-FC measures which exhibit a hierarchical preference. One such measure is global brain connectivity (GBC) (Cole et al., 2010). Here, we adapted GBC to parcellated rs-FC matrices. The GBC of region i was defined as the average FC between region i and the rest of the regions:

$$GBC_i = \frac{1}{N}\sum_{j \neq i}^{N}\left(FC_{ij}\right) \quad (55)$$

where N is the number of brain regions. GBC is equivalent to the graph-theoretic measure of node strength normalized by total number of nodes.

To provide mechanistic insight into the model-generated GBC, we compared the patterns of model GBC to the SC node degree (Baria et al., 2013), and to the eigenvector of the slowest mode. We calculated the SC node degree as the sum of non-zero connections of each brain area, after binarizing the SC matrix using a threshold ($T = 10^{-5}$ for the normalized SC matrix) (Figure S6).

Inter-Individual Dissimilarity—To characterize variation in rs-FC patterns of each region across subjects, we adapted inter-individual variability as proposed in Mueller et al. (2013). Since this measure reflects the dissimilarity across rs-FC patterns, we refer to it as a measure of dissimilarity instead of variability. In empirical data, we refer to the measure as inter-individual dissimilarity, whereas in the model, we refer to it as inter-particle dissimilarity. The inter-individual/particle dissimilarity V_i is calculated as:

$$V_i = E\left[1 - corr\left(F_i\left(s_p\right), F_i\left(s_q\right)\right)\right], \quad p \neq q \quad (56)$$

where $F_i(s)$ is a vector of rs-FC values between region i and rest of the regions in subject/particle s, $corr(x,y)$ is the Spearman rankcorrelation between variables x and y, and $E[.]$ denotes expected value. Due to the analytical approximation of the model FCs, the scales of

inter-individual and inter-particle dissimilarity were different. To normalize the scales of both measures, we z-scored the final spatial maps of inter-individual/particle dissimilarity. Of note, cross-subject alignment in MMSAll registration is limited by atypical topologies, and therefore some portion of inter-individual dissimilarity is attributable to mis-registration of areas to the atlas (Robinson et al., 2014).

In addition to inter-individual dissimilarity, we characterized the standard deviations of each connection in empirical and model FC, calculated across subjects for empirical and across particles for model. Then, we calculated the similarities between the empirical and model standard deviation FC matrices.

Spectral Characterization of the Model—As described in Deco et al. (2014), the power spectrum of the model can be analytically approximated around its fixed points. The cross-spectrum Φ as a function of frequency ω can be calculated by:

$$\mathbf{\Phi}(\omega) = \sigma^2 (\mathbf{A} + i\omega\mathbf{I})^{-1} \left(\mathbf{A}^{\mathbf{T}} - i\omega\mathbf{I}\right)^{-1} \quad (57)$$

where A is the Jacobian of the system of synaptic variables described by Equations 4–8, σ is the standard deviation of the input noise, i is $\sqrt{-1}$, and $\mathbf{I}$ is the identity matrix.

The power spectral density (PSD) was computed as the diagonal elements of $\mathbf{\Phi}(\omega)$ for frequencies $\omega \in (0.01, \ldots, 75 \text{ Hz})$. The PSDs of left and right hemisphere models were normalized by dividing by total PSD. The PSDs were reported in dB ($10\log_{10}$).

To study the role of long-range connections on the behavior of the system, we estimated the PSDs of the model without long-range connections (Figure S7). Briefly, we replaced the term S_j^E in Equation 4 with a constant current set to the average excitatory synaptic gating variable $\langle S^E \rangle$, such that the long-range connection term reduced to an external synaptic input, i.e., $I_{ext} = gJ\langle S^E \rangle$.

Principal Component Analysis of Empirical and Model Power Spectral Density—We applied principal component analysis (PCA) to the group-averaged MEG PSDs across cortical areas (Mellem et al., 2017; Hill-ebrand et al., 2012; Martín-Buro et al., 2016) (Figures 7 and S8). The PSDs were log-transformed so that the data are in units of dB. Prior to PCA, the PSDs were normalized across areas by parcel-averaged spectral power of each frequency, so that they expressed fractional deviation from the mean. Then PCA was applied to this data matrix $\mathbf{X}$ whose axes are parcel by frequency (size: 360 samples $\times$ 48 features). PCA yielded principal axes (as eigenvectors of the data covariance matrix) in the frequency feature space. Principal axis 1 is therefore the spectral pattern which captures the most spectral variance across areas. We define the principal components (PCs) as the coordinates of the data expressed in the basis of corresponding principal axes. PC-1 is therefore the areal map whose values are the loadings of spectral variation for each area onto principal axis 1. PC-1 maps were compared to the T1w/T2w map. For both homogeneous and heterogeneous models, we used the same data analysis procedure to extract the first principal components,

in the same frequency range as the empirical data (3–50 Hz). We repeated the same analysis using raw (i.e., without alpha/beta components removed) MEG PSD relative power maps, and after removal of alpha, or alpha and beta, Lorentzians (Figure S8). We also performed PCA over the model PSDs in a broader frequency range (0–75 Hz) (Figure S8).

Numerical Simulations—To show the validity of the analytical approximation of BOLD FC and PSD, we employed full simulations of the model. We integrated synaptic Equations 4–8 and BOLD Equations 11–14 using Euler method with $dt = 0.1$ ms. The input noise levels were defined as $\sigma = 10^{-5}$. This input noise level was chosen to avoid noise-induced destabilization of the system as it approaches a bifurcation. To calculate BOLD FC, we simulated the BOLD signals for 870 s to match experimental recording sessions. The first 6 s of simulations were discarded to ensure that the system's state converges to the neighborhood of the baseline fixed point. The simulated BOLD signals were down-sampled using 0.72 s resolution resulting in 1200 TRs as in the single–session empirical BOLD data from the HCP. To calculate simulated PSDs, we simulated the excitatory synaptic gating variables for 170 s, and later downsampled to 10 ms after removing the first 6 s of simulations. In total, 10 simulations were performed for 20 random iterations using particles that were drawn from the posterior distribution.

To assess the role of noise in numerical simulations we concatenated the simulated time series (after z-scoring across time points), and calculated the simulated BOLD FC for different scan times. The similarity between simulated and analytical BOLD FC rose to $r = 0.972 \pm 0.005$ for the simulations with 4800 TR (≈ 1 h; matching the duration of 4 sessions of empirical BOLD time series in HCP data).

The same simulation protocol was repeated using synaptic delays. The distance between brain regions was defined by the average pairwise Euclidean distance between two parcels. The conductance velocity was defined as $v = 6$ m/s, which is consistent with empirically observed values (Horowitz et al., 2015).

QUANTIFICATION AND STATISTICAL ANALYSIS

As a statistical test for the difference between similarities of the measures derived from homogeneous and heterogeneous models to the empirical data, we employed the dependent correlation test. The dependent correlations test provides a non-parametric test to compare the correlations of two variables against a common dependent variable based on bootstrapping (Wilcox, 2016). The dependent correlation tests were employed directly when Spearman rank correlation was used as a measure of similarity (i.e., GBC and BLP). When Pearson correlation was used as a measure of similarity (i.e., FC, within-/across-network FC, inter-individual/particle dissimilarity), skipped Pearson correlation was used to perform dependent correlation tests due to sensitivity of Pearson correlation to possible outliers during bootstrapping. However, using Pearson correlation instead of skipped Pearson correlation did not change the results.

To assess the improvement in explanatory power of each model with respect to SC alone, we constructed a linear regression model to predict empirical FC such that ($Y^{(full)}$):

$$Y^{(full)} = \beta_0 + \beta_{sc}X_{sc} + \beta_{model}X_{model} + \text{error} \quad (58)$$

We compared the variation explained by the full model to the reduced model, in which the empirical FC is predicted by only SC ($Y^{(reduced)}$):

$$Y^{(reduced)} = \beta_0 + \beta_{sc}X_{sc} + \text{error} \quad (59)$$

We calculated the coefficient of partial determination (CPD) as:

$$CPD = \frac{SS^{(reduced)} - SS^{(full)}}{SS^{(reduced)}} \quad (60)$$

The CPD is the proportion of variation that cannot be explained by the reduced model, but can be explained by the full model.

To test for differences between the average measures in sensory and association areas in empirical data (i.e., T1w/T2w maps, GBC, inter-individual dissimilarity), we used the Wilcoxon signed-rank test. The Wilcoxon signed-rank test provides a non-parametric measure for the difference between the ranks of repeated measurements of two related samples.

The surrogate heterogeneity maps were used to generate various sample null distributions for statistics (e.g., model FC fitting). Reported significance values were calculated as the proportion of samples in the null distributions whose values exceeded that of the test statistic.

DATA AND SOFTWARE AVAILABILITY

All results derive from the publicly available HCP dataset. Parcellated maps and connectivity matrices related to this study are available via the BALSA database (https://balsa.wustl.edu/). Custom modeling and analysis codes written in Python are available at https://github.com/murraylab/hbnm.

Supplementary Material

Refer to Web version on PubMed Central for supplementary material.

ACKNOWLEDGMENTS

REFERENCES

Anselin L (2001). Spatial econometrics In A Companion to Theoretical Econometrics, Baltagi BH, ed. (Blackwell), pp. 310–330.

Baker JT, Holmes AJ, Masters GA, Yeo BTT, Krienen F, Buckner RL, and Öngür D (2014). Disruption of cortical association networks in schizophrenia and psychotic bipolar disorder. JAMA Psychiatry 71, 109–118. [PubMed: 24306091]

Baria AT, Mansour A, Huang L, Baliki MN, Cecchi GA, Mesulam MM, and Apkarian AV (2013). Linking human brain local activity fluctuations to structural and functional network architectures. Neuroimage 73, 144–155. [PubMed: 23396160]

Beaumont MA, Cornuet JM, Marin JM, and Robert CP (2009). Adaptive approximate Bayesian computation. Biometrika 96, 983–990.

Breakspear M (2017). Dynamic models of large-scale brain activity. Nat. Neurosci 20, 340–352. [PubMed: 28230845]

Burt JB, Demirta M, Eckner WJ, Navejar NM, Ji JL, Martin WJ, Bernacchia A, Anticevic A, and Murray JD (2018). Hierarchy of transcriptomic specialization across human cortex captured by structural neuroimaging topography. Nat. Neurosci 21, 1251–1259. [PubMed: 30082915]

Chaudhuri R, Knoblauch K, Gariel MA, Kennedy H, and Wang XJ (2015). A large-scale circuit mechanism for hierarchical dynamical processing in the primate cortex. Neuron 88, 419–431. [PubMed: 26439530]

Chaudhuri R, He BJ, and Wang XJ (2018). Random recurrent networks near criticality capture the broadband power distribution of human ECoG dynamics. Cereb. Cortex 28, 3610–3622. [PubMed: 29040412]

Cole MW, Pathak S, and Schneider W (2010). Identifying the brain's most globally connected regions. Neuroimage 49, 3132–3148. [PubMed: 19909818]

Cole MW, Anticevic A, Repovs G, and Barch D (2011). Variable global dysconnectivity and individual differences in schizophrenia. Biol. Psychiatry 70, 43–50. [PubMed: 21496789]

Cole MW, Yarkoni T, Repovs G, Anticevic A, and Braver TS (2012). Global connectivity of prefrontal cortex predicts cognitive control and intelligence. J. Neurosci 32, 8988–8999. [PubMed: 22745498]

Cole MW, Bassett DS, Power JD, Braver TS, and Petersen SE (2014). Intrinsic and task-evoked network architectures of the human brain. Neuron 83, 238–251. [PubMed: 24991964]

Deco G, Jirsa VK, and McIntosh AR (2011). Emerging concepts for the dynamical organization of resting-state activity in the brain. Nat. Rev. Neurosci 12, 43–56. [PubMed: 21170073]

Deco G, Ponce-Alvarez A, Mantini D, Romani GL, Hagmann P, and Corbetta M (2013). Resting-state functional connectivity emerges from structurally and dynamically shaped slow linear fluctuations. J. Neurosci 33, 11239–11252. [PubMed: 23825427]

Deco G, Ponce-Alvarez A, Hagmann P, Romani GL, Mantini D, and Corbetta M (2014). How local excitation-inhibition ratio impacts the whole brain dynamics. J. Neurosci 34, 7886–7898. [PubMed: 24899711]

Dombrowski SM, Hilgetag CC, and Barbas H (2001). Quantitative architecture distinguishes prefrontal cortical systems in the rhesus monkey. Cereb. Cortex 11, 975–988. [PubMed: 11549620]

Donahue CJ, Sotiropoulos SN, Jbabdi S, Hernandez-Fernandez M, Behrens TE, Dyrby TB, Coalson T, Kennedy H, Knoblauch K, Van Essen DC, and Glasser MF (2016). Using diffusion tractography to predict cortical connection strength and distance: a quantitative comparison with tracers in the monkey. J. Neurosci 36, 6758–6770. [PubMed: 27335406]

Elston GN (2003). Cortex, cognition and the cell: new insights into the pyramidal neuron and prefrontal function. Cereb. Cortex 13, 1124–1138. [PubMed: 14576205]

Felleman DJ, and Van Essen DC (1991). Distributed hierarchical processing in the primate cerebral cortex. Cereb. Cortex 1, 1–47. [PubMed: 1822724]

Finn ES, Shen X, Scheinost D, Rosenberg MD, Huang J, Chun MM, Papademetris X, and Constable RT (2015). Functional connectome finger-printing: identifying individuals using patterns of brain connectivity. Nat. Neurosci 18, 1664–1671. [PubMed: 26457551]

Frauscher B, von Ellenrieder N, Zelmann R, Dole zalová I, Minotti L, Olivier A, Hall J, Hoffmann D, Nguyen DK, Kahane P, et al. (2018). Atlas of the normal intracranial electroencephalogram: neurophysiological awake activity in different cortical areas. Brain 141, 1130–1144. [PubMed: 29506200]

Freyer F, Roberts JA, Becker R, Robinson PA, Ritter P, and Breakspear M (2011). Biophysical mechanisms of multistability in resting-state cortical rhythms. J. Neurosci 31, 6353–6361. [PubMed: 21525275]

Friston KJ, Harrison L, and Penny W (2003). Dynamic causal modelling. Neuroimage 19, 1273–1302. [PubMed: 12948688]

Glasser MF, and Van Essen DC (2011). Mapping human cortical areas in vivo based on myelin content as revealed by T1- and T2-weighted MRI.J. Neurosci 31, 11597–11616. [PubMed: 21832190]

Glasser MF, Sotiropoulos SN, Wilson JA, Coalson TS, Fischl B, Andersson JL, Xu J, Jbabdi S, Webster M, Polimeni JR, et al.; WU-Minn HCP Consortium (2013). The minimal preprocessing pipelines for the Human Connectome Project. Neuroimage 80, 105–124. [PubMed: 23668970]

Glasser MF, Goyal MS, Preuss TM, Raichle ME, and Van Essen DC (2014). Trends and properties of human cerebral cortex: correlations with cortical myelin content. Neuroimage 93, 165–175. [PubMed: 23567887]

Glasser MF, Coalson TS, Robinson EC, Hacker CD, Harwell J, Yacoub E, Ugurbil K, Andersson J, Beckmann CF, Jenkinson M, et al. (2016). A multi-modal parcellation of human cerebral cortex. Nature 536, 171–178. [PubMed: 27437579]

Greicius MD, Supekar K, Menon V, and Dougherty RF (2009). Resting-state functional connectivity reflects structural connectivity in the default mode network. Cereb. Cortex 19, 72–78. [PubMed: 18403396]

Hagmann P, Cammoun L, Gigandet X, Meuli R, Honey CJ, Wedeen VJ, and Sporns O (2008). Mapping the structural core of human cerebral cortex. PLoS Biol. 6, e159. [PubMed: 18597554]

Heinzle J, Koopmans PJ, den Ouden HEM, Raman S, and Stephan KE (2016). A hemodynamic model for layered BOLD signals. Neuroimage 125, 556–570. [PubMed: 26484827]

Hernández M, Guerrero GD, Cecilia JM, García JM, Inuggi A, Jbabdi S, Behrens TEJ, and Sotiropoulos SN (2013). Accelerating fibre orientation estimation from diffusion weighted magnetic resonance imaging using GPUs. PLoS ONE 8, e61892. [PubMed: 23658616]

Hilgetag CC, Medalla M, Beul SF, and Barbas H (2016). The primate connectome in context: Principles of connections of the cortical visual system. Neuroimage 134, 685–702. [PubMed: 27083526]

Hillebrand A, Barnes GR, Bosboom JL, Berendse HW, and Stam CJ (2012). Frequency-dependent functional connectivity within resting-state networks: an atlas-based MEG beamformer solution. Neuroimage 59, 3909–3921. [PubMed: 22122866]

Honey CJ, Sporns O, Cammoun L, Gigandet X, Thiran JP, Meuli R, and Hagmann P (2009). Predicting human resting-state functional connectivity from structural connectivity. Proc. Natl. Acad. Sci. USA 106, 2035–2040. [PubMed: 19188601]

Honey CJ, Thesen T, Donner TH, Silbert LJ, Carlson CE, Devinsky O, Doyle WK, Rubin N, Heeger DJ, and Hasson U (2012). Slow cortical dynamics and the accumulation of information over long timescales. Neuron 76, 423–434. [PubMed: 23083743]

Horowitz A, Barazany D, Tavor I, Bernstein M, Yovel G, and Assaf Y (2015). In vivo correlation between axon diameter and conduction velocity in the human brain. Brain Struct. Funct 220, 1777–1788. [PubMed: 25139624]

Hughes SW, and Crunelli V (2005). Thalamic mechanisms of EEG alpha rhythms and their pathological implications. Neuroscientist 11, 357–372. [PubMed: 16061522]

Huntenburg JM, Bazin PL, Goulas A, Tardif CL, Villringer A, and Margulies DS (2017). A systematic relationship between functional connectivity and intracortical myelin in the human cerebral cortex. Cereb. Cortex 27, 981–997. [PubMed: 28184415]

Ito T, Kulkarni KR, Schultz DH, Mill RD, Chen RH, Solomyak LI, and Cole MW (2017). Cognitive task information is transferred between brain regions via resting-state network topology. Nat. Commun 8, 1027. [PubMed: 29044112]

Jbabdi S, Sotiropoulos SN, Savio AM, Graña M, and Behrens TEJ (2012). Model-based analysis of multishell diffusion MR data for tractography: how to get over fitting problems. Magn. Reson. Med 68, 1846–1855. [PubMed: 22334356]

Kasper L, Bollmann S, Diaconescu AO, Hutton C, Heinzle J, Iglesias S, Hauser TU, Sebold M, Manjaly ZM, Pruessmann KP, and Stephan KE (2017). The physio toolbox for modeling physiological noise in fMRI data.J. Neurosci. Methods 276, 56–72. [PubMed: 27832957]

Keitel A, and Gross J (2016). Individual human brain areas can be identified from their characteristic spectral activation fingerprints. PLoS Biol. 14, e1002498. [PubMed: 27355236]

Kucyi A, Schrouff J, Bickel S, Foster BL, Shine JM, and Parvizi J (2018). Intracranial electrophysiology reveals reproducible intrinsic functional connectivity within human brain networks. J. Neurosci 38, 4230–4242. [PubMed: 29626167]

Larson-Prior LJ, Oostenveld R, Della Penna S, Michalareas G, Prior F, Babajani-Feremi A, Schoffelen JM, Marzetti L, de Pasquale F, Di Pompeo F, et al.; WU-Minn HCP Consortium (2013). Adding dynamics to the Human Connectome Project with MEG. Neuroimage 80, 190–201. [PubMed: 23702419]

Margulies DS, Ghosh SS, Goulas A, Falkiewicz M, Huntenburg JM, Langs G, Bezgin G, Eickhoff SB, Castellanos FX, Petrides M, et al. (2016). Situating the default-mode network along a principal gradient of macro-scale cortical organization. Proc. Natl. Acad. Sci. USA 113, 12574–12579. [PubMed: 27791099]

Markov NT, Vezoli J, Chameau P, Falchier A, Quilodran R, Huissoud C, Lamy C, Misery P, Giroud P, Ullman S, et al. (2014). Anatomy of hierarchy: feedforward and feedback pathways in macaque visual cortex. J. Comp. Neurol 522, 225–259. [PubMed: 23983048]

Martín-Buro MC, Garcés P, and Maestú F (2016). Test-retest reliability of resting-state magnetoencephalography power in sensor and source space. Hum. Brain Mapp 37, 179–190. [PubMed: 26467848]

Mateo C, Knutsen PM, Tsai PS, Shih AY, and Kleinfeld D (2017). Entrainment of arteriole vasomotor fluctuations by neural activity is a basis of blood-oxygenation-level-dependent "resting-state" connectivity. Neuron 96, 936–948.e3. [PubMed: 29107517]

Mejias JF, Murray JD, Kennedy H, and Wang XJ (2016). Feedforward and feedback frequency-dependent interactions in a large-scale laminar network of the primate cortex. Sci. Adv 2, e1601335. [PubMed: 28138530]

Mellem MS, Wohltjen S, Gotts SJ, Ghuman AS, and Martin A (2017). Intrinsic frequency biases and profiles across human cortex. J. Neurophysiol 118, 2853–2864. [PubMed: 28835521]

Mueller S, Wang D, Fox MD, Yeo BTT, Sepulcre J, Sabuncu MR, Shafee R, Lu J, and Liu H (2013). Individual variability in functional connectivity architecture of the human brain. Neuron 77, 586–595. [PubMed: 23395382]

Murray JD, Bernacchia A, Freedman DJ, Romo R, Wallis JD, Cai X, Padoa-Schioppa C, Pasternak T, Seo H, Lee D, and Wang XJ (2014). A hierarchy of intrinsic timescales across primate cortex. Nat. Neurosci 17, 1661–1663. [PubMed: 25383900]

Murray JD, Jaramillo J, and Wang XJ (2017). Working memory and decision-making in a frontoparietal circuit model. J. Neurosci 37, 12167–12186. [PubMed: 29114071]

Murray JD, Demirta M, and Anticevic A (2018). Biophysical modeling of large-scale brain dynamics and applications for computational psychiatry. Biol. Psychiatry Cogn. Neurosci. Neuroimaging 3, 777–787. [PubMed: 30093344]

Obata T, Liu TT, Miller KL, Luh WM, Wong EC, Frank LR, and Buxton RB (2004). Discrepancies between BOLD and flow dynamics in pri-mary and supplementary motor areas: application of the balloon model to the interpretation of BOLD transients. Neuroimage 21, 144–153. [PubMed: 14741651]

Power JD, Plitt M, Laumann TO, and Martin A (2017). Sources and implications of whole-brain fMRI signals in humans. Neuroimage 146, 609–625. [PubMed: 27751941]

Preller KH, Burt JB, Ji JL, Schleifer C, Adkinson B, Stämpfli P, Seifritz E, Repovs G, Krystal JH, Murray JD, Vollenweider FX, and Anticevic A. (2018). Changes in global and thalamic brain connectivity in LSD-induced altered states of consciousness are attributable to the 5-HT2A receptor. eLife 7, e35082. [PubMed: 30355445]

Robinson EC, Jbabdi S, Glasser MF, Andersson J, Burgess GC, Harms MP, Smith SM, Van Essen DC, and Jenkinson M (2014). MSM: a new flexible framework for multimodal surface matching. Neuroimage 100, 414–426. [PubMed: 24939340]

Salvador R, Suckling J, Schwarzbauer C, and Bullmore E (2005). Undirected graphs of frequency-dependent functional connectivity in whole brain networks. Philos. Trans. R. Soc. Lond. B Biol. Sci 360, 937–946. [PubMed: 16087438]

Schölvinck ML, Maier A, Ye FQ, Duyn JH, and Leopold DA (2010). Neural basis of global resting-state fMRI activity. Proc. Natl. Acad. Sci. USA 107, 10238–10243. [PubMed: 20439733]

Sotiropoulos SN, Jbabdi S, Xu J, Andersson JL, Moeller S, Auerbach EJ, Glasser MF, Hernandez M, Sapiro G, Jenkinson M, et al.; WU-Minn HCP Consortium (2013). Advances in diffusion MRI acquisition and processing in the Human Connectome Project. Neuroimage 80, 125–143. [PubMed: 23702418]

Sotiropoulos SN, Hernández-Fernández M, Vu AT, Andersson JL, Moeller S, Yacoub E, Lenglet C, Ugurbil K, Behrens TEJ, and Jbabdi S (2016). Fusion in diffusion MRI for improved fibre orientation estimation: An application to the 3T and 7T data of the Human Connectome Project. Neuroimage 134, 396–409. [PubMed: 27071694]

Turner BM, and Van Zandt T (2014). Hierarchical approximate Bayesian computation. Psychometrika 79, 185–209. [PubMed: 24297436]

Van Essen DC, Smith SM, Barch DM, Behrens TEJ, Yacoub E, and Ugurbil K; WU-Minn HCP Consortium (2013). The WU-Minn Human Connectome Project: an overview. Neuroimage 80, 62–79. [PubMed: 23684880]

Wilcox RR (2016). Comparing dependent robust correlations. Br. J. Math. Stat. Psychol 69, 215–224. [PubMed: 27114391]

Wong KF, and Wang XJ (2006). A recurrent network mechanism of time integration in perceptual decisions. J. Neurosci 26, 1314–1328. [PubMed: 16436619]

Yang GJ, Murray JD, Repovs G, Cole MW, Savic A, Glasser MF, Pittenger C, Krystal JH, Wang XJ, Pearlson GD, et al. (2014). Altered global brain signal in schizophrenia. Proc. Natl. Acad. Sci. USA 111, 7438–7443. [PubMed: 24799682]

Yang GJ, Murray JD, Wang XJ, Glahn DC, Pearlson GD, Repovs G, Krystal JH, and Anticevic A (2016). Functional hierarchy underlies preferential connectivity disturbances in schizophrenia. Proc. Natl. Acad. Sci. USA 113, E219–E228. [PubMed: 26699491]

Zimmermann J, Griffiths J, Schirner M, Ritter P, and McIntosh AR (2019). Subject-specificity of the correlation between large-scale structural and functional connectivity. Network Neuroscience 3, 90–106. [PubMed: 30793075]

Highlights

- A circuit model with areal heterogeneity across cortex is fit to resting-state fMRI

- Hierarchical specialization of microcircuitry follows the MRI-derived T1w/T2w map

- T1w/T2w provides a preferential axis of specialization to fit functional connectivity

- Hierarchical specialization is an organizing principle for spatiotemporal dynamics
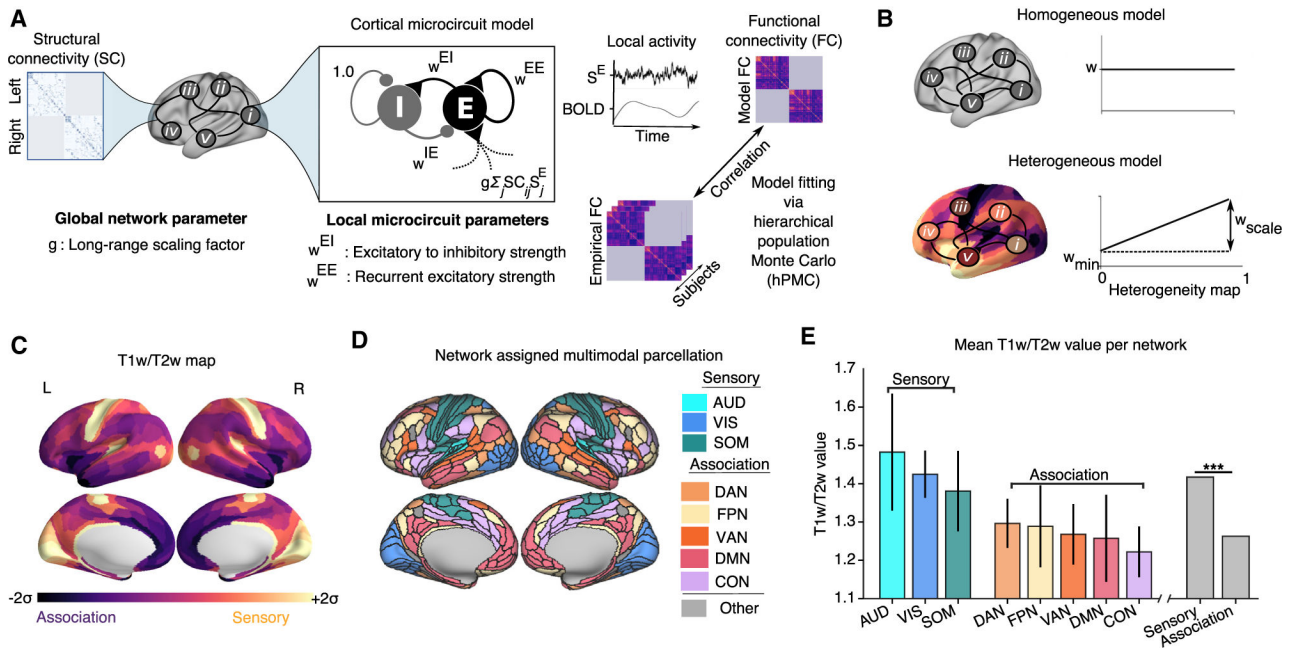
Figure 1. Large-Scale Model of Human Cortex with Heterogeneous Local Circuit Properties

(A) Model framework. Each parcellated cortical area is modeled as coupled excitatory (E) and inhibitory (I) populations. Areas interact through long-range projections following dMRI-derived intra-hemispheric structural connectivity (SC). Fit model parameters comprised recurrent excitatory strength (W^{EE}), excitatory-to-inhibitory strength (W^{EI}), and a global coupling parameter scaling the strength of long-range connections (g). Inhibitory-to-excitatory strengths (W^{IE}) were adjusted to maintain a uniform baseline excitatory firing rate across areas. Dynamics of synaptic gating variables (S^E) are transformed into a simulated BOLD signal via the Balloon-Windkessel hemodynamic model. For computational tractability of model fitting, model BOLD FC matrices were calculated via linearization of the extended dynamical equations around the fixed point of the system. Model parameters were fit to maximize the similarity between model and empirical FC matrices.

(B) Parametrizing local properties via a heterogeneity map. In the homogeneous model, the parameters (W^{EI} and W^{EE}) were identical across cortical regions. In the heterogeneous model, the parameters (W^{EI} and W^{EE}) varied across cortical areas based on a heterogeneity map h, whose minimum and maximum value is 0 and 1, respectively. For each region (i), the parameter values were set by an affine function of the heterogeneity map values $\{h_i\}$, characterized by an intercept W_{min} and scale factor W_{scale}: $W_i = W_{min} + W_{scale}h_i$.

(C) Cortical T1w/T2w map. The median ($n = 334$ subjects) cortical T1w/T2w map values of each parcellated cortical area (180 per hemisphere).

(D) Network assignments. Cortical areas were assigned to eight functional resting-state networks (RSNs) comprising three sensory (AUD, auditory; VIS, visual; and SOM, somatomotor) and five association (DAN, dorsal attention; FPN, frontoparietal; VAN, ventral attention; DMN, default mode; and CON, cinguloopercular) networks.

(E) T1w/T2w map values per RSN, averaged across areas. T1w/T2w values are significantly lower in association RSNs than in sensory RSNs ($p < 0.003$, Wilcoxon signed-rank test,

difference between sensory and association T1w/T2w across subjects). Error bars indicate the SD across areas within an RSN.
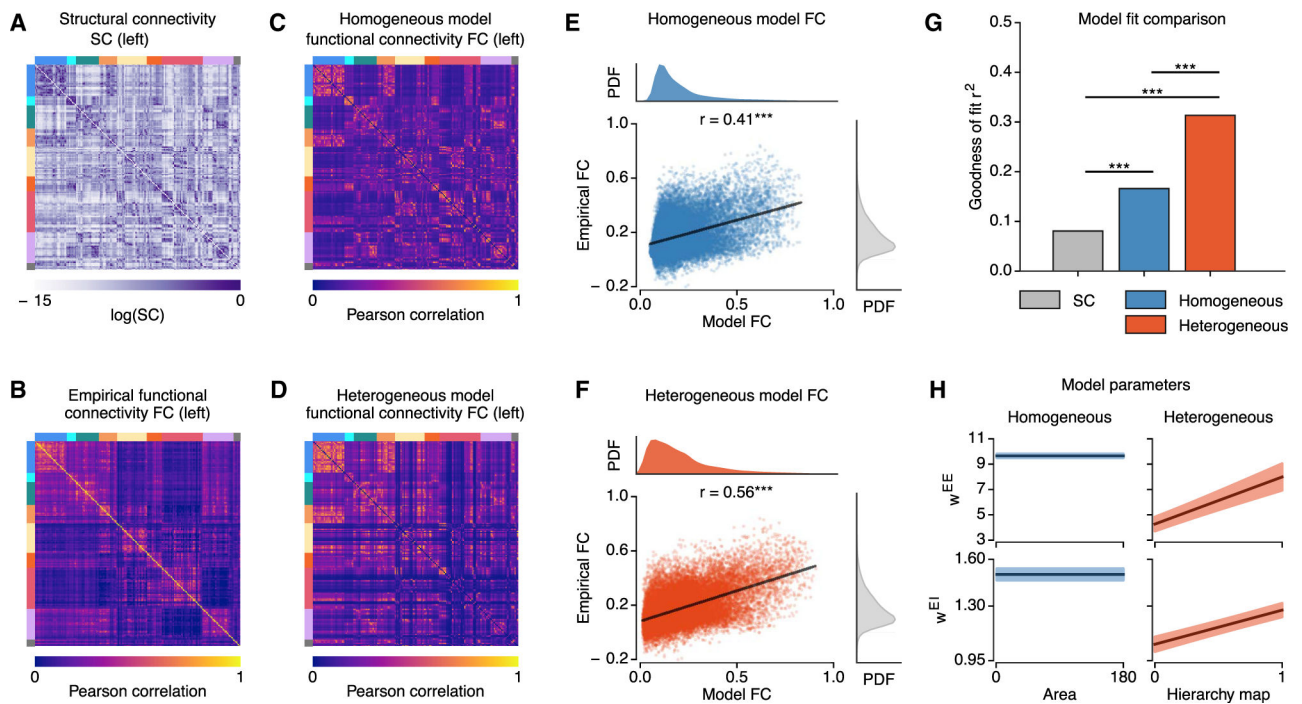
Figure 2. Hierarchical Heterogeneity Improves the Model Fit to rs-FC

(A and B) Structural connectivity (SC) (A) and empirical FC (B) matrices (left hemisphere only), averaged across subjects. Colored bars (top and left of matrices) denote resting-state network assignments (colored as in Figure 1).

(C and D) Model FC of the homogeneous (C) and heterogeneous (D) models (left hemisphere only), averaged across particles (***,$p < 10^{-3}$).

(E and F) Correlation between average empirical FC and average model FC for the homogeneous (E) and heterogeneous (F) models.

(G) Goodness of fit (i.e., fraction of explained variance r^2) between the average empirical FC and the SC (gray), homogeneous model FC (blue), and heterogeneous model FC (red). The fit for the heterogenous model is greater than that of the homogeneous model, which is greater than that of the SC ($p < 10^{-5}$ for each, dependent correlation test).

(H) The best-fit values for recurrent excitatory parameters for the models, with regions ordered by increasing values of the T1w/T2w-derived hierarchical heterogeneity map. Shaded regions show SD across particles.
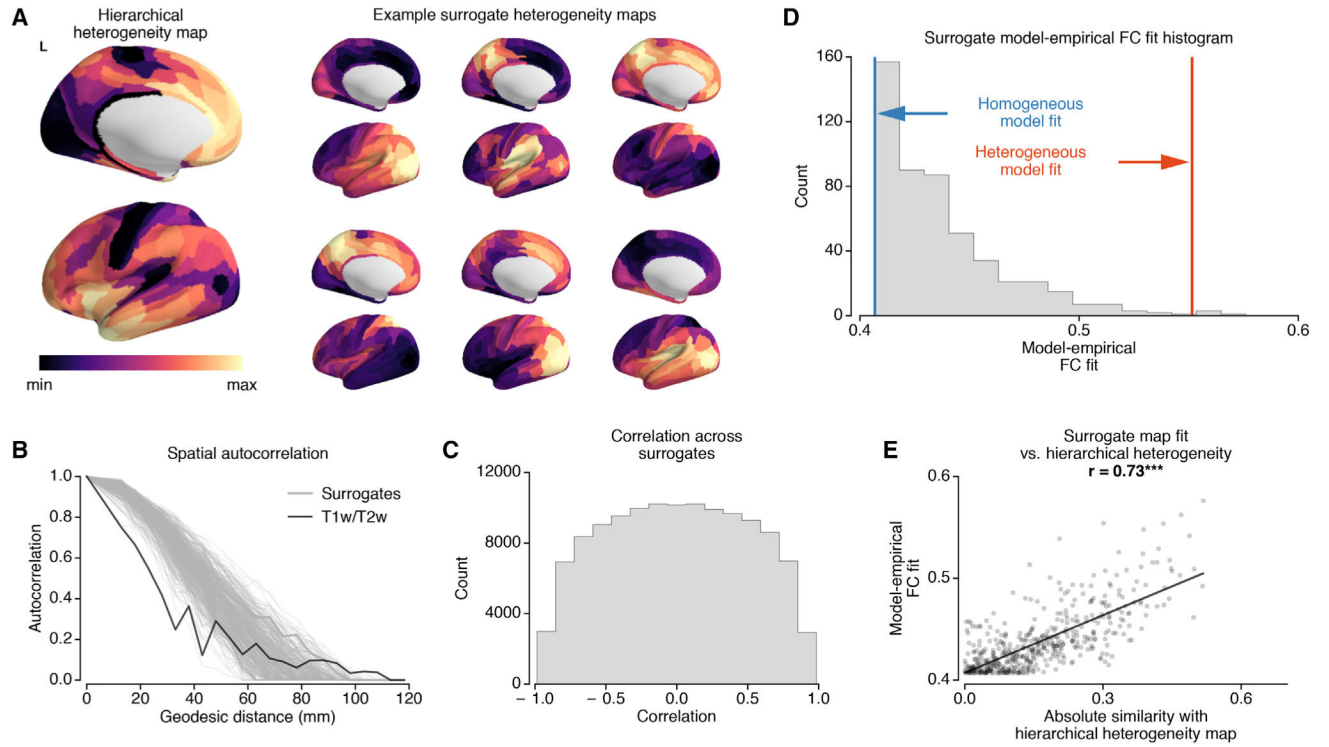
Figure 3. Surrogate Heterogeneity Maps Show that the T1w/T2w Map Provides a Preferential Axis of Specialization

(A) The T1w/T2w-based hierarchical heterogeneity map, for the left hemisphere, and example surrogate heterogeneity maps with matched spatial autocorrelations.

(B) Spatial autocorrelations of the Box-Cox-transformed T1w/T2w map (black) and surrogate heterogeneity maps (gray) as a function of geodesic distance.

(C) Histogram of spatial correlations (Spearman rank) between all pairs of random surrogate maps.

(D) Histogram of the best fit (correlation between empirical and model FC) of random surrogates. The T1w/T2w map gradient fit is significantly higher than random surrogates ($p = 0.008$).

(E) The correlation between hierarchical heterogeneity-surrogate map similarity (i.e., absolute values of correlation) and model performance (i.e., model-empirical FC similarity). The model-empirical FC similarities for surrogate maps increase with the absolute value of the correlation with the hierarchical heterogeneity map ($r = 0.73$, $p < 10^{-3}$).
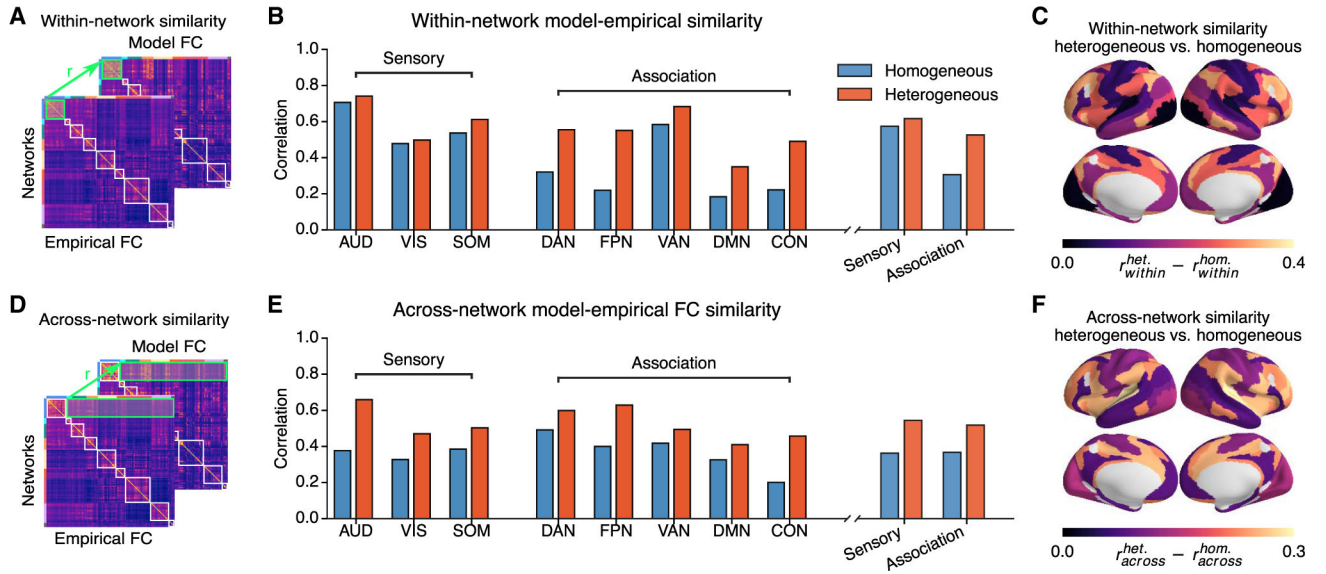
Figure 4. Model Fits across Resting-State Networks Are Network Specific

(A and D) Schematic of within- and across-network fits. Correlations between empirical and model FC within or between RSNs were calculated for homogeneous and heterogeneous models.

(B and E) Within-network (B) and across-network (E) fits of the models. The heterogeneous model showed substantial improvements compared to the homogeneous model, for within- and across-networks fit in all networks. Across-network fit improvements were distributed across sensory and association networks. Within-network fit improvements were preferentially in association networks.

(C and F) Topography of the improvement in fit for within-network (C) and across-network (F). Values are shown for each RSN.
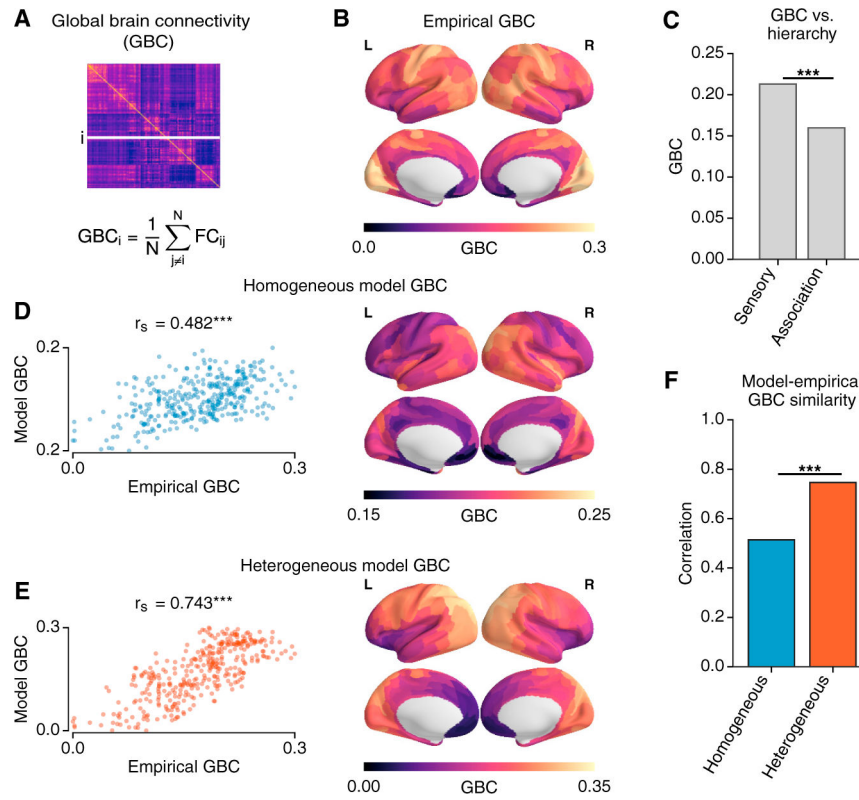
Figure 5. Hierarchical Topography of Cortical GBC

(A) GBC of each region is calculated as the average FC of that region with all other cortical regions.

(B) The areal topography of empirical GBC.

(C) GBC of sensory areas is significantly larger than that of association areas ($p < 0.001$, Wilcoxon signed-rank test).

(D–F) The correlation between empirical and model GBC is significantly larger in the heterogeneous(D) model than for the homogeneous (E) model ($p < 10^{-4}$, dependent correlation test; ***, $p < 10^{-3}$).
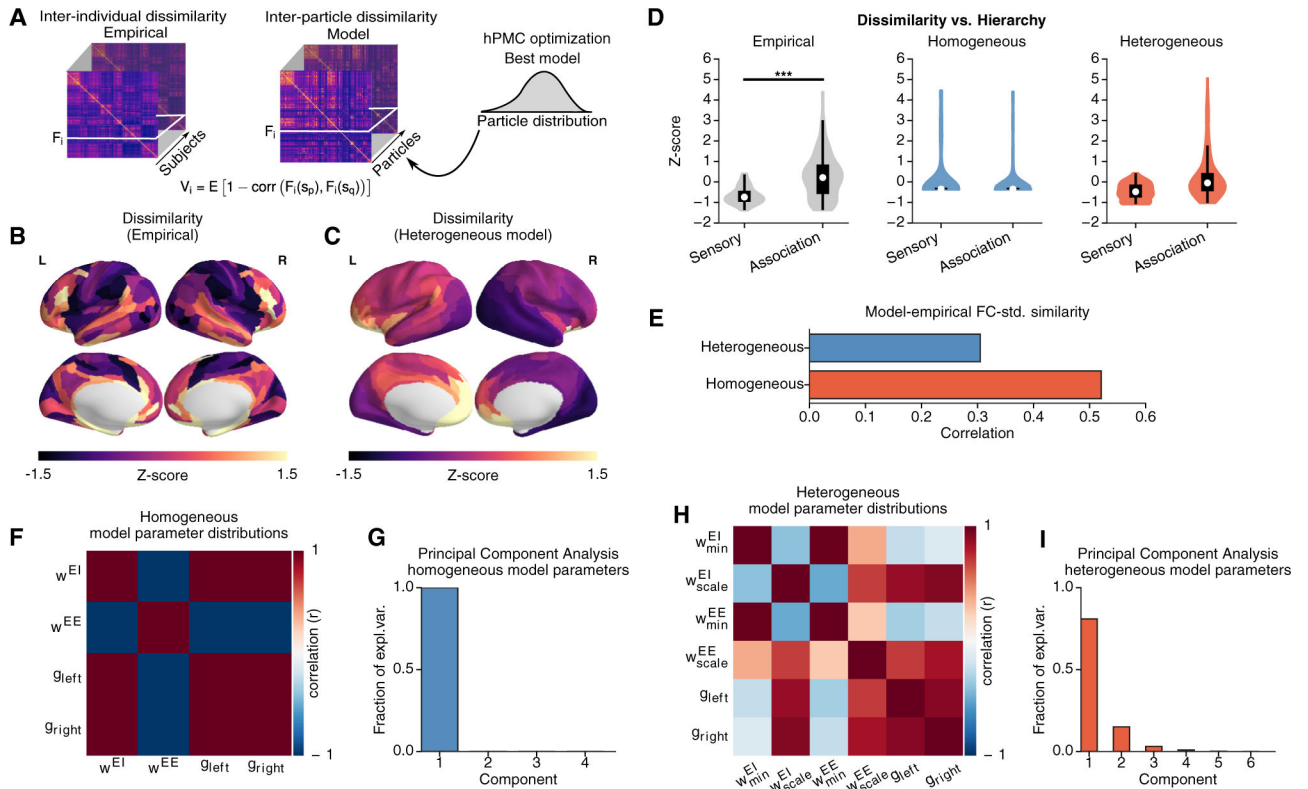
Figure 6. Hierarchical Topography of Inter-individual Dissimilarity of FC

(A) Dissimilarity calculated for FC patterns across subjects ($n = 334$) in the empirical dataset and across particles (n = 1, 000) in the model fitting framework. The dissimilarity for area i, V_i, is given by $V_i = E(1 - Corr(F_i(s_p), F_i(s_q)))$, where $E(\ldots)$. is the mean across subject pairs and $F_i(s_p)$ is the FC of area i for subject s_p. To compare the areal topographies of empirical and model dissimilarity maps, we standardize the values through Z score.

(B and C) Topography of empirical inter-individual dissimilarity (B) and heterogeneous model inter-particle dissimilarity (C). The inter-particle dissimilarity for the homogeneous model was not depicted due to lack of spatial patterns.

(D) Inter-individual dissimilarity is higher for association areas than for sensory areas ($p < 0.003$, Wilcoxon signed-rank test). The heterogeneous model exhibits a similar hierarchical differentiation in inter-particle dissimilarity. The association-sensory difference is larger in the heterogeneous model than homogeneous ($p < 10^{-4}$, 2×2 ANOVA, $z = 5.3$).

(E) Similarity between empirical and model SD of FC across subjects (particles).

(F and H) Correlations between parameters, across particles in the approximate posterior distributions, for the homogeneous (F) and heterogeneous (H) models. Homogeneous model parameters are very strongly correlated with each other.

(G and I) PCA applied to the distribution of particles drawn from the posterior, with their parameter values normalized by the population mean for each parameter. Plotted is the fraction of explained variance by the top PCs. 100% of the variation in homogeneous model parameters is explained by a single dimension (G). The variation in the heterogeneous model is explained by four components (I).
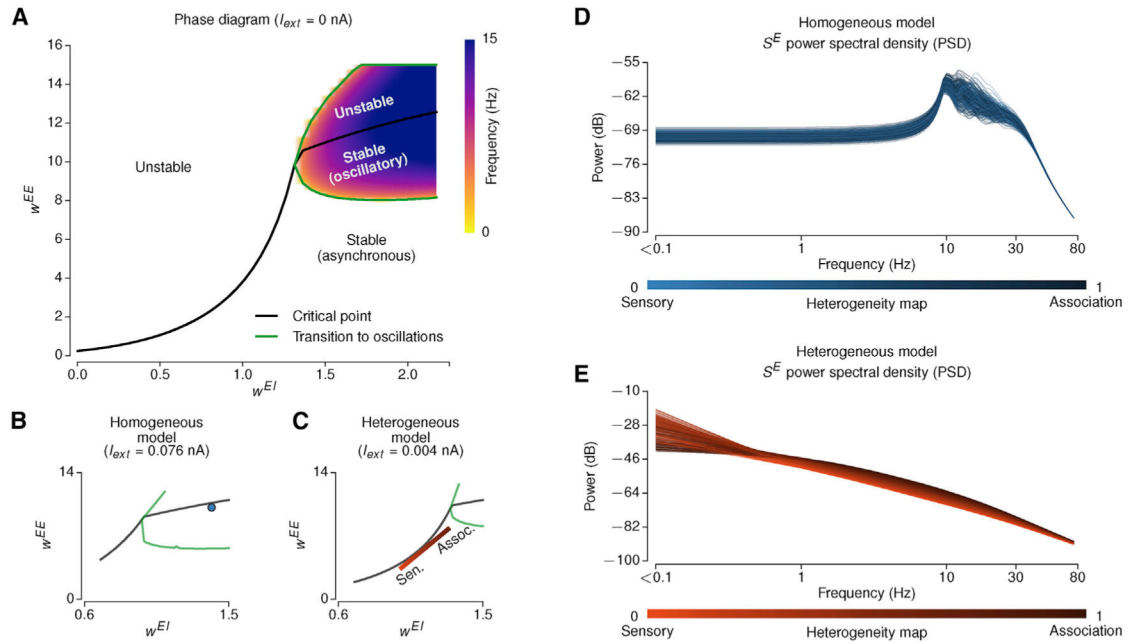
Figure 7. Intrinsic Dynamics of a Local Microcircuit Model Vary with Recurrent Strengths

(A) The phase diagram of a local microcircuit model (i.e., one node in the large-scale network) without external input. The black line indicates the critical points beyond which the baseline state is unstable, and the green lines indicate the boundaries at which the system exhibits a transition to oscillatory dynamics. For excitatory-to-inhibitory synaptic strengths (W^{EI}) smaller than 1.35, the system exhibits a pitchfork bifurcation (in asynchronous dynamics), and for larger W^{EI} values, the system exhibits a transition to damped oscillatory dynamics.

(B and C) A representative example of optimal homogeneous (B) and heterogeneous (C) model parameters projected onto the phase diagram. The external input is adjusted to provide the same mean long-range input as in the fit large-scale model from other areas.

(D and E) The power spectral densities (PSDs) of the synaptic gating variables (S^E) of the homogeneous (D) and heterogeneous (E) models. The colors indicate the hierarchical level of each area based on its T1w/T2w map value (light, sensory; dark, association).
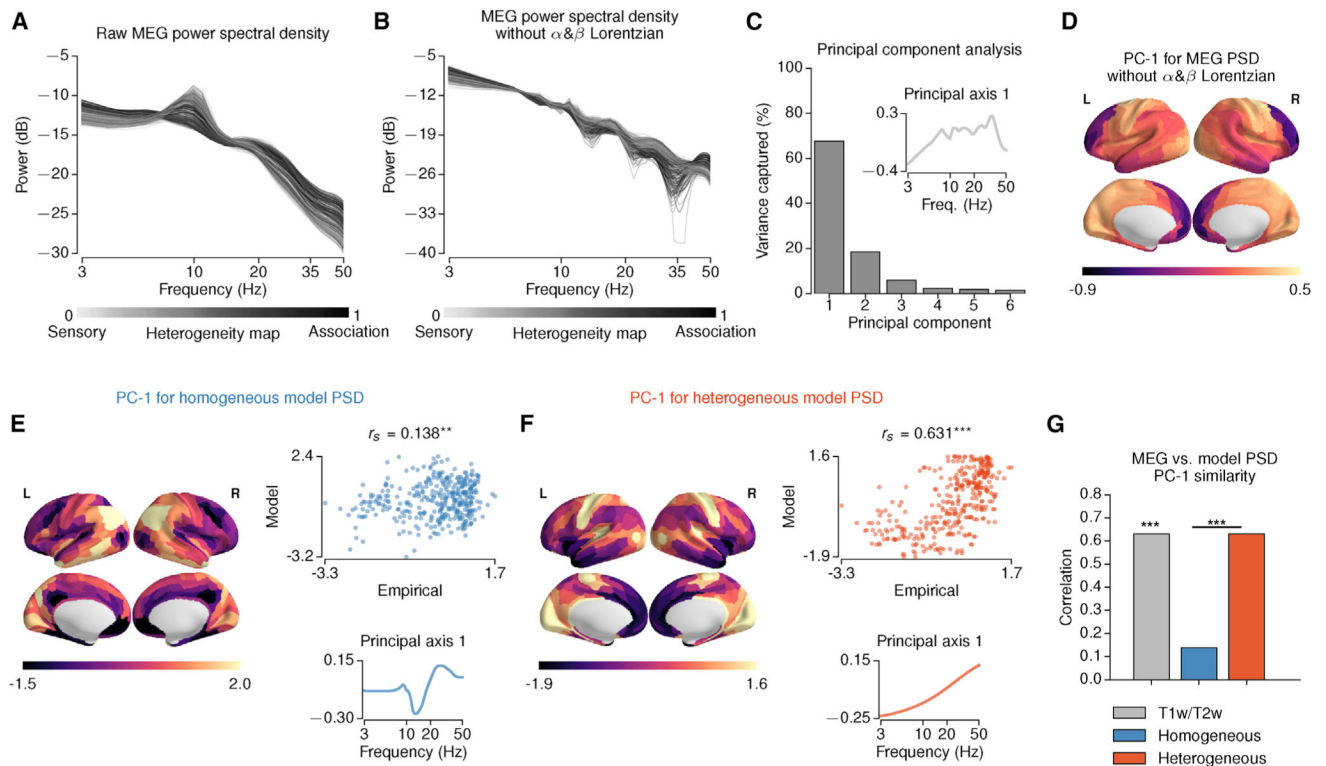
Figure 8. Hierarchical Topography of Spectral Power in MEG

(A and B) The empirical PSD derived from raw MEG (A) and with removal of alpha-band (α) and beta-band (β) Lorentzians (B). The shading of lines indicates values of the T1w/T2w-based hierarchical heterogeneity map.

(C and D) PCA applied to empirical MEG PSDs, with removal of α and β Lorentzians. The first principal axis is the spectral pattern that captures the most spectral variation across areas (C) inset. The first principal component (PC-1) is the areal map whose values are the loading of the spectral variation for each area onto the first principal axis (D). PC-1 captures 67.5% of the total spectral variance (C).

(E and F) PCA results for the homogeneous (E) and heterogeneous (F) models and comparison to the empirical PC-1 map. Left: spatial topography of the model MEG PSD PC-1. Right, top: correlation between model and empirical PC-1 map topographies. Right, bottom: principal axis 1 (**,$p < 10^{-2}$; ***, $p < 10^{-3}$).

(G) Spearman correlation of the empirical MEG PSD PC-1 map with T1w/T2w, and model PSD PC-1 maps. The empirical MEG PSD PC-1 map is significantly correlated with T1w/T2w ($r_s = 0.631, p = 0.002$, against 500 randomized surrogate maps). The correlation of the model PSD PC-1 map with the T1w/T2w map is higher for the heterogeneous model than the homogeneous model.

Table 1.

Fixed Parameter Values for Synaptic and Hemodynamics Equations in the Model

	Excitatory Populations	Inhibitory Populations
Synaptic model parameters		
I_b	0.382 nA	-
J	0.15 nA	-
γ	0.641	-
W^E	1.0	-
τ^E	0.1 s	-
a^E	310 nC^{-1}	-
b^E	125 Hz	-
d^E	0.16 s	-
W^I	-	0.7
τ^I	-	0.01 s
a^I	-	615 nC^{-1}
b^I	-	177 Hz
d^I	-	0.087 s
Hemodynamic model parameters		
ρ	0.34	-
a	0.32	-
V_0	0.02	-
γ	0.41 s^{-1}	-
κ	0.65 s^{-1}	-
k_1	3.72	-
k_2	0.53	-
k_3	0.53	-

Table 2.

Prior Distributions for hPMC Model Fitting

Parameter (θ)	Homogeneous	Heterogeneous
W^{EI}_{min}	U(0.001, 5.0)	U(0.001, 2.0)
W^{EE}_{min}	U(0.001, 15.0)	U(0.001, 5.0)
$g_k g_r$	U(0.001, 5.0)	U(0.001, 2.0)
W^{EI}_{scale}	-	U(0, 2.5)
W^{EE}_{scale}	-	U(0, 15.0)

U(MIN, MAX) denotes a uniform probability distribution between the minimum (MIN) and maximum (MAX).

Key Resources Table

REAGENT or RESOURCE	SOURCE	IDENTIFIER
Software and Algorithms		
Heterogeneous brain network model simulation and fitting software	This paper	https://github.com/murraylab/hbnm
Connectome Workbench pipeline	Connectome Coordination Facility	https://www.humanconnectome.org/software/connectome-workbench
MEG Connectome pipeline	Connectome Coordination Facility	https://www.humanconnectome.org/software/hcp-meg-pipelines
FieldTrip	Donders Institute for Brain, Cognition and Behaviour	http://www.fieldtriptoolbox.org